

Photodissociation and rotational excitation of interstellar CO

S. Warin¹, J.J. Benayoun¹, and Y.P. Viala^{2,3}

¹ Observatoire de Grenoble, Laboratoire d'Astrophysique, Université Joseph Fourier, B.P.53X, F-38041, Grenoble Cedex, France

² Observatoire de Paris, DEMIRM, 61 avenue de l'Observatoire, F-75014 Paris, France

³ Ecole Normale Supérieure, Radioastronomie, 24 rue Lhomond, F-75231 Paris Cedex 05, France

Received 16 May 1995 / Accepted 31 August 1995

Abstract. We have developed a detailed interstellar cloud model that takes into account the chemistry among simple carbon and oxygen bearing molecules, as well as ^{13}C and ^{18}O isotopic compounds. The rotational population of H_2 , CO, ^{13}CO and C^{18}O and the fine structure excitation of C, C^+ and O are controlled by chemical processes, including selective photodissociation which depends on the rotational quantum number J , collisional and radiative processes allowing for photon trapping of CO millimeter and sub-millimeter lines. The gas and grain temperature distributions are obtained by solving a thermal equilibrium equation for each component. Comparison with the previous model calculations of van Dishoeck & Black (1988) and Le Bourlot et al. (1993) are made throughout the paper.

We have computed series of models for three kinds of quiescent interstellar clouds: diffuse, translucent and dense dark clouds. The variations of the photodissociation rates are mainly controlled by self-shielding effects leading to a rotational selective photodissociation, i.e. a strong dependence on the rotational quantum number J : the more populated the level the more efficient is the self-shielding and the more rapid is the decrease of its photodissociation rate. This implies a strong coupling between photodissociation and rotational excitation, which has for main consequence to overpopulate low-lying levels and to underpopulate excited levels with respect to an LTE calculation. Under the combined influence of the rotational photodissociation and the inefficiency of collisions to populate excited levels, at the densities and temperatures prevailing in most clouds, the rotational population of CO and its isotopes is sub-thermally excited, except for the first two rotational levels of the three isotopes and the levels $J = 2$ and 3 of the main isotope which are thermalized in the inner part of dark clouds.

Photo-electric emission of electrons from grains is the dominant heating process in regions where UV photons are present, i.e. in diffuse and translucent clouds and in the outer parts of dark clouds. It is replaced by cosmic ray ionization of atomic and molecular hydrogen as a dominant heating process in the core of dark clouds. The cooling efficiency is entirely correlated to the cloud composition, with cooling dominated by fine

structure excitation of C^+ and rotational excitation of CO in diffuse and dark clouds, respectively; fine structure excitation of C contributes to the cooling of translucent clouds. The strong dependence of the temperature distribution in interstellar clouds on the external UV radiation field is emphasized.

Our model calculations have been confronted with selected CO surveys of molecular clouds by Frerking et al. (1982), Cericharo & Guélin (1987) and Lada et al. (1994). For that purpose, we have run series of model with various visual extinctions and densities covering a large range of values, from diffuse to dense cloud conditions. The temperature distribution was obtained by solving the thermal balance equation. The model predicts emissivities of the $1 \rightarrow 0$ line of CO well below the observations with the exception of the $\text{C}^{18}\text{O}(1 \rightarrow 0)$ line in the molecular clouds surveyed by Frerking et al. (1982) for which agreement between theory and observations is very good. Although the model predicts too low abundances of both ^{13}CO and C^{18}O , the column density ratio $R(^{13}\text{CO}/\text{C}^{18}\text{O})$ normalized to the isotopic ratio that we compute is in fairly good qualitative agreement with the one derived by Lada et al (1994) in the IC 5146 molecular cloud. The model calculations have also been used to predict the emissivities of the CO, ^{13}CO , C^{18}O , C and C^+ lines under various interstellar conditions.

Key words: ISM: molecules – ISM: clouds general – molecular processes – radio lines: ISM

1. Introduction

Since the discovery of its first rotational transition $J = 1 \rightarrow 0$ in emission, the CO molecule has proved to be a very powerful tool to probe physical and chemical conditions in various types of molecular clouds, the densest and coldest parts of the interstellar medium and the sites of star formation. Owing to the low energy spacing between its rotational levels and also its low dipole moment, CO can be rather easily excited, even at very low temperatures of a few Kelvins and at fairly low densities down to a few hundred particles/cm³. Hence rotational emission

Send offprint requests to: S. Warin

of CO, including excited transitions (e.g. $J = 2 \rightarrow 1, 3 \rightarrow 2\dots$), has been predicted to be detectable and has actually been observed in a fairly large range of densities, temperatures and UV radiation fields encountered in the interstellar medium. The possibility to observe several rotational transitions is furthermore very useful to set up diagnostics on the physical state of the gas.

The observed transitions of CO are mainly excited by collisions with the hydrogen molecule, the presence of which is furthermore necessary to form CO, as all other molecules so far detected in interstellar space. Hence, the emission of CO lines indicates the presence of H₂ molecules, and this is of particular importance, since H₂ which is the most abundant molecule in interstellar gas is very difficult to observe, because it has no permanent dipole moment in its ground electronic state and also because the energy spacing between its rotational levels is too large for these levels to be easily excited. Due to the widespread chemical and physical conditions allowing observation of CO, it is a very good tracer of molecular gas in our galaxy as well as in external galaxies. Rotational lines from the main isotope ¹²C¹⁶O are generally intense but optically thick and even saturated; they allow to probe only the outer envelopes of molecular clouds and are mainly used to locate and to map the molecular gas. Lines from the rarer isotopes ¹³C¹⁶O and ¹²C¹⁸O have also been detected, weaker but nearly as widespread as those of the main isotope. These lines, and particularly those of ¹²C¹⁸O, are assumed to be optically thin and are hence more useful to probe the core of molecular clouds. From observations of fairly large samples of molecular clouds in the Milky Way and in nearby galaxies, more or less strong correlations have been found between integrated intensity of the $1 \rightarrow 0$ and $2 \rightarrow 1$ lines of the three main isotopes of CO and visual extinction and/or H₂ column densities, so that observations of CO lines are very often used to derive the mass of molecular gas.

Because of its astrophysical importance and thanks to a large number of theoretical works, the chemistry of the CO molecule has been studied in a great variety of physical conditions. Chemical processes controlling the abundance of CO and its isotopes appeared to be well understood and the sensitivity of the CO abundance to its physical environment was rather well established. In particular, the fact that CO was fairly abundant and detected in nearly all kinds of interstellar clouds, even the most diffuse ones, was explained by a strong resistance to photo-destruction by UV radiation. However, the photodissociation cross section was poorly known and this was the main uncertainty in modeling the chemistry of CO and its isotopes. This lack of information has been removed these last few years through high-resolution spectroscopic measurements of the absorption spectrum of CO in the far UV (Letzelter et al. 1987; Yoshino et al. 1988; Eidelberg & Rostas 1990, Stark et al. 1991). These studies have shown the existence of many excited Rydberg electronic states and revealed that the photodissociation of CO occurs through absorption of photons in rotational lines from the ground vibrational level towards these excited electronic states, most of them being entirely predissociated.

Using these new spectroscopic data, the problem of the photodissociation rate and abundance of CO in interstellar clouds

has been re-addressed by Viala et al. (1988a) (hereafter VLER) and van Dishoeck & Black (1988) (hereafter VDB), while Mamon et al. (1988) and Nercessian et al. (1989) built models of circumstellar envelopes. In the first two studies on interstellar clouds, the dependence of the photodissociation rate in each individual rotational line with depth within clouds has been accounted for. To do this, the radiation field as a function of wavelength within the line and as a function of depth within the cloud was computed by solving a transfer equation which takes into account all absorbers, as it is described in Sect. 2 below. More recently, in a paper mainly concerned with prediction of the emissivities of atomic and molecular cooling lines from interstellar clouds, Le Bourlot et al. (1993) (hereafter LPRF) also treated explicitly the dependence of CO photodissociation with depth within the cloud. In most of their calculations, the line photodissociation rate was computed with the simplified theory of Federman, Glassgold & Kwan (1979) which, instead of solving the transfer problem as a function of frequency within the line, introduces a self-shielding function that gives, after integration over frequency, an approximated line absorption coefficient, which assumes that only the line itself contributes to absorption of photons. This approximation of course reduces considerably the computing time but it has the major inconvenience of neglecting the shielding by neighbouring lines which increases as the depth within the cloud increases and, in any case, becomes important for shielding of CO lines by H₂ lines and shielding of lines of the rare isotopes ¹³CO and C¹⁸O by lines of ¹²CO, as discussed later.

Apart from a large enhancement of the total photodissociation rate of CO in the unshielded interstellar UV radiation field by a factor of 20 with respect to previous estimations, the theoretical studies mentioned above put in evidence another important feature: the efficiency of self shielding. The consequence is a fairly rapid decrease of the photodissociation rate with depth, more rapid than in the case of continuum dissociation.

The influence of spectroscopic parameters such as the oscillator strength of the transition and the lifetime of the upper levels on the variations of the line photodissociation rates with optical depth have been discussed in detail by VLER. This first study however treated only the main isotope ¹²C¹⁶O and did not consider the rotational excitation of the molecule which was assumed to be in its ground rotational level $J = 0$.

A more complete model including the rarer isotopes and taking into account the photodissociation from excited rotational level has been presented by VDB. In this model however, the overall photodissociation rate of CO, averaged over the first ten rotational levels, was computed in an approximate way by assuming that the rotational population is characterized by a single excitation temperature. The problem is in fact somewhat more complicated because the photodissociation of CO occurs through absorption of photons in individual rotational lines. Indeed, due to the self-shielding efficiency, the photodissociation rate of each rotational level at a given point within a cloud will strongly depend on the column density of that level from the cloud surface to the current point, and, conversely, the population of the level is controlled by its photodissociation rate.

Therefore, UV photodissociation and more generally chemical processes forming or destroying CO and its isotopes, will affect their rotational population, besides radiative and collisional processes.

This point, together with the improvements of the spectroscopic data that have been accomplished since the first theoretical works mentioned above, led us to present new model calculations on the photodissociation, abundance and rotational excitation of CO and its isotopes ^{13}CO and C^{18}O . The model only applies to quiescent interstellar molecular clouds, excluding shocks and photodissociation regions. All processes susceptible to modify the rotational population have been taken into account: chemical processes, selective photodissociation of rotational levels, collisional excitation and de-excitation and radiative processes, i.e. absorption, spontaneous and stimulated emission of rotational transitions. Concerning radiative processes, the possibility that photons can be trapped within the medium, as the optical depths of the transitions become large, has been taken into account by the model. The rotational population of H_2 is also treated by the model along the way described in Viala et al. (1988b) by including UV pumping through excited electronic states. The model of the chemistry, the photodissociation and the rotational excitation of CO is presented in Sect. 2. Sect. 3 studies the contribution of the different bands to the photodissociation rates as well as self-shielding and mutual shielding effects. In Sect. 4 the model is then applied to compute the photodissociation rates, the abundances and the rotational populations of CO and its isotopes throughout interstellar clouds. Results are presented for three types of molecular clouds: diffuse, translucent and dark ones. Comparison with observations, mainly the surveys of four molecular clouds is made in Sect. 5. Our main conclusions are given in Sect. 6.

2. Rotational excitation of interstellar CO

The equation governing the population of a particular rotational level of CO (or its isotopes) can be written, in its more general form:

$$\begin{aligned} n_j \left\{ A_{j,j-1} + B_{j,j-1} J_{j,j-1} + \zeta_j^{\text{diss}} + \sum_q n_q k_{qj} \right\} + \\ n_j \left\{ \sum_p n_p \left(\sum_{i < j} C_{ji}^p + \sum_{k > j} C_{kj}^p \right) \right\} = \\ n_{j+1} (A_{j+1,j} + B_{j+1,j} J_{j+1,j}) + n_{j-1} B_{j-1,j} J_{j-1,j} \\ + \sum_{k > j} n_k \sum_p n_p C_{kj}^p + \sum_{i < j} n_i \sum_p n_p C_{ij}^p \\ + \sum_r \sum_s p_j^{rs} k_{rs} n_r n_s \end{aligned} \quad (1)$$

In this relation, n_i , n_j and n_k are the densities of the molecule in level i , j and k respectively, where j denotes the level under consideration of energy E_j , while i and k represent levels below ($E_i < E_j$) and above ($E_k > E_j$) level j . The n_p are the densities of species which undergo collisions with CO, leading to excitation or de-excitation of rotational levels. The

n_q , n_r and n_s are the densities of species which are involved in chemical reactions destroying or forming CO. The left hand side and right hand side of Eq. (1) give the destruction and formation rates of level j , respectively.

The first two terms of the left hand side represent the radiative processes that destroy level j , i.e. the spontaneous and stimulated emission towards the level $i = j - 1$. J_{ji} is the mean specific intensity of the transition $j \rightarrow i$, integrated over frequency within the line, and A_{ji} and B_{ji} are the usual Einstein coefficients. The two following terms are the destruction rate of level j due to absorption of UV photons and chemical reactions with species q . The last terms give the destruction rate of level j by collisions with species p , it is the sum of collisional de-excitations and excitations towards lower and upper levels, respectively.

The first two terms of the right hand side represent the radiative processes that populate level j , the first one is the sum of the spontaneous and stimulated emissions from the upper level $k = j + 1$ and the second one correspond to absorption of radiation from the lower level $i = j - 1$. The two following terms give the rate at which level j is populated through collisional de-excitations from upper levels and through collisional excitations from lower levels. The last term is the rate at which chemical reactions form the molecule in level j , p_j^{rs} being the probability that the chemical reaction between species r and s form the molecule in rotational level j .

The set of Eqs. (1) represent the usual statistical equilibrium equations to which we have added the photodissociation and chemical processes. The influence of these last processes on the rotational population is discussed in Sect. 4 below.

Apart from CO, the model also treats the rotational excitation within the ground vibrational level of the H_2 molecule. We follow here what has been done in a previous work: the set of equations to be solved are Eqs. (41) and (42) from Viala et al. (1988b). Equation (41) that governs the rotational population of H_2 is similar to Eq. (1) above in the sense that it contains radiative, collisional, chemical processes and selective photodissociation of rotational levels, but it includes another important process: UV pumping through absorption of radiation towards excited electronic states followed by radiative decay towards the ground state leading either to dissociation or to radiative cascades within this state down to the rotational levels of the ground vibrational level. UV pumping through excited electronic state, can also, in principle alter the rotational population of CO. However, it was not included in the work presented here (data about radiative cascades within the ground electronic state were not available when we started this work).

2.1. Radiative processes, photon trapping and emergent intensities

The radiative transition probability for a CO transition $J \rightarrow J - 1$ is given by (electric dipole transition within a ${}^1\Sigma$ state):

$$A_{J,J-1} = \frac{64 \pi^4 \nu_{J,J-1}^3}{3hc^3} \mu^2 \frac{J}{2J+1} \quad (2)$$

or

$$C_{ji} = a_0 + a_1 \exp(-T/\alpha) + a_2 \exp(-2T/\alpha) + a_3 \exp(-3T/\alpha) \quad (11)$$

the coefficients a_i and α , the range of temperatures as well as the references of theoretical studies in which collisional cross-sections and rates were determined, are given in Appendix A. The rates given by the two relations above are accurate to better than 10 %. The collisional excitation rates are obtained from the de-excitation ones through the usual balance equation:

$$C_{ij} = \frac{g_j}{g_i} \exp\left(-\frac{E_j - E_i}{kT}\right) C_{ji} \quad (12)$$

where $g_J = 2J+1$ is the statistical weight of the rotational level.

Collisional rates for the isotopes ^{13}CO and C^{18}O have been assumed identical to those of the main isotope. Collisional excitation of these three species, followed by emission of photons escaping the cloud, are important contributors to the cooling of the gas (see below), at least in its densest and coolest parts. In hotter and more diffuse parts, the cooling comes primarily from fine structure excitation of atomic species such as C, C^+ and O. Collisional rates for these species and references are also given in Appendix A, as well as those for H_2 .

2.3. Photodissociation processes

Since the first studies that addressed the question of the photodissociation and abundance of interstellar and circumstellar CO, using data obtained from high resolution spectroscopy of CO in the far UV, progresses have been made in this last field, leading to significant improvements of the data (Eidelsberg & Rostas 1990).

New upper electronic states have been identified for the four main isotopes. Spectroscopic parameters such as band head frequencies and rotational constants have been determined, leading to accurate frequencies of rotational transitions from the ground level towards these excited states. This is important in the context of mutual shielding of CO lines by H_2 lines.

Spectroscopic identification of the excited levels has been performed and their vibrational assignment has been obtained. This point, as discussed below, is of particular importance to determine the amount of shielding of the rarer isotopes by the main one.

Absorption cross sections and fluorescence measurements were continued, in particular for the ^{13}CO and C^{18}O isotopes, and led to the determination of the band oscillator strength in absorption and the dissociation probability of the upper state.

Finally, evaluation of the lifetimes of the excited Rydberg states has been slightly improved through a combined evaluation of the width of the rotational lines, of the fluorescence yield and of the variation of the band absorption cross section with pressure.

Thanks to this laboratory work, an atlas of the absorption lines of the four main isotopes of CO in the far UV has been

achieved (Eidelsberg et al. 1991, 1992). Extracted from this atlas, Table 1 lists the spectroscopic parameters of the absorption bands of CO, ^{13}CO and C^{18}O . For the main isotope, 49 absorption bands have been identified; the 46 of them that lead to nearly complete predissociation are listed in the table. For comparison, the values adopted by VDB are also given. It is worth noting that, since VDB's model calculations, 13 new bands have been identified; differences in lifetime estimations are also significant, as well as in vibrational assignment, since Table 1 lists more excited vibrational levels ($v > 0$) than in the VDB's study.

The 49 upper vibrational Rydberg states that have been identified for $^{12}\text{C}^{16}\text{O}$ also exist for the rarer isotopes but have not all been observed. They have however been included in Table 1 since they do contribute to the photodissociation of these rarer isotopes. The adopted parameter values come from the UV atlas (Eidelsberg et al. 1991, 1992). More recent data for oscillator strengths and dissociation probabilities have been obtained (Leveld et al. 1992a,b; Stark et al. 1992, 1993; Drabbels et al. 1993; Morton & Noreau 1994; Yoshino et al. 1995). These new molecular data will probably not change significantly the results presented hereafter. The dissociation probabilities for the rarer isotopes are not listed in the table because they have been assumed identical to those of the main isotope. Estimated lifetimes are also identical except for 5 levels which are given as footnotes to the table.

All these spectroscopic data allow fairly precise determination of photodissociation rates in individual lines connecting each rotational level J of the ground vibrational level to a predissociated rotational level J' belonging to an excited electronic Rydberg state. The overall photodissociation rate of a particular rotational level J is obtained by summing over all lines starting from that level:

$$\zeta_J = \sum_{J'} p_{J'} \frac{\pi e^2}{m_e c} f_{JJ'} \int \phi_{JJ'}(\nu) 4\pi J(r, \nu) d\nu \quad (13)$$

In this equation, $p_{J'}$ is the probability that the upper level dissociates, it is taken from Table 1 and we assumed that all rotational levels belonging to the same vibrational upper state have the same dissociation probability. $f_{JJ'}$ is the line absorption oscillator strength which can be derived from the band oscillator strength $f_{vv'}$ and the band head frequency ν_0 listed in Table 1:

$$f_{JJ'} = f_{vv'} \frac{\nu_{JJ'}}{\nu_0} \frac{S_J}{2J+1} \quad (14)$$

where the line frequency $\nu_{JJ'}$ is taken from the UV atlas and S_J is the Hönl-London factor of the transition ($S_J = J$ or $J+1$ for a P or R branch of a $\Sigma \rightarrow \Sigma$ transition, and $S_J = (J-1)/2$, $(2J+1)/2$ or $(J+2)/2$ for a P , Q or R branch of a $\Sigma \rightarrow \Pi$ transition). For the normalized line profile $\phi(\nu)$ we adopted a Voigt profile with a Doppler contribution including microturbulent broadening, as for millimeter and sub-millimeter lines, and a Lorentzian contribution, which dominates in the line wings and varies as the reciprocal lifetime of the upper level; here again, all rotational levels of the same upper vibrational level are assumed to have the same value τ listed in Table 1. As far as the

photodissociation of CO is concerned, the Lorentzian part of the profile is very important since it gives the major contribution to the line photodissociation rate as the optical depth in the cloud increases. The influence of the lifetime of the upper level on the line photodissociation rate and its variation with depth within clouds has been discussed in VLER: The lower the lifetime, i.e. the more diffuse appears the band, and the largest is the line photodissociation rate as the optical depth increases. Despite the improvements in lifetime estimations mentioned above, it remains the less well determined parameter with an uncertainty of about half an order of magnitude. The effects of varying this parameter on the results of model calculations is discussed in Sect. 4 below.

The flux of photons (in number of photons $\text{cm}^{-2} \text{s}^{-1} \text{Hz}^{-1}$) $4\pi J(z, \nu)$ is computed as a function of frequency within each rotational line. This is obtained by solving a transfer equation which takes into account absorption by dust grains and by the gas along the way described in VLER. Assuming a plane parallel geometry for a cloud of finite thickness, the mean intensity of the UV radiation field is given by

$$J(z, \nu) = \frac{1}{2} J_0(\nu) \{ E_2 [2\tau_{tot}(z, \nu) - \tau(z, \nu)] + E_2 [\tau(z, \nu)] \} \quad (15)$$

where $\tau(z, \nu)$ is the dust plus gas opacity measured at the current point r from the nearest cloud surface:

$$\begin{aligned} \tau(z, \nu) = & \sum_i N_i(z) \sigma_i(\nu) + \\ & \sqrt{1 - \omega(\nu)} \frac{R E(B-V)}{1.086 N_H} \left(1 + \frac{1}{R} \frac{E(\lambda-V)}{E(B-V)} \right) n(z) \end{aligned} \quad (16)$$

The external radiation field $J_0(\nu)$ is taken from Mathis et al. (1983) as well as the dust grain albedo $\omega(\nu)$ and the dust grain extinction curve $E(\lambda-V)/E(B-V)$ for which we use the values adopted for their grain mixture composition. For the ratio of total to selective extinction and the gas-to-dust ratio we adopt the “canonical values” $R = 3.1$ and $N_H/E(B-V) = 5.8 \times 10^{21} \text{ cm}^{-2} \text{mag}^{-1}$. For each line (CO and H₂) a uniform grid-point in frequency is adopted, with a constant spacing corresponding to $8 \times 10^{-4} \text{ \AA}$, i.e. $1/25^{\text{th}}$ of a Doppler width for a turbulent broadening velocity of 1 km s^{-1} , and the integration over frequency within the line is performed up to 10^4 Doppler widths apart from the line centre. At each frequency within each line, the gas absorption coefficient given by the last term of Eq. (16) includes all possible absorbers: the line itself, all H (Lyman series), H₂ (Lyman and Werner bands) and CO lines whose frequencies lie at less than 10 \AA from the current frequency, atoms (mainly carbon) and molecules whose photoionization and photodissociation occur in the same wavelength range. Line overlap and mutual shielding is hence properly accounted for by the model and its importance is discussed in Sect. 4 below.

2.4. Chemical processes

The chemical reaction scheme involves simple molecules (up to 4 atoms) formed from H, C and O elements. It is mainly

the one adopted in Viala (1986) in which all reactions involving nitrogen compounds have been deleted, assuming implicitly that reactions with these species do not strongly affect the abundances of carbon and oxygen bearing molecules. Since this first publication, several rate coefficients have been either newly measured or re-determined, especially at low temperature. We used here this new determinations, taken from the compilation by Anicich (1993). Since we are interested in the formation and destruction processes of ¹³CO and C¹⁸O, besides those of CO, and since the ¹³C- and ¹⁸O- isotopic substitutions of the simple chemical species considered here are involved in these processes, their chemistry has been added to the chemical scheme. This has been done by merely duplicating the reactions involving C and O bearing species, but we restricted ourselves to isotopic species containing only one of the rare isotope ¹³C or ¹⁸O.

We also added to the library of chemical reactions the eight following reactions: ¹³C⁺ + ¹²CO \leftrightarrow ¹²C⁺ + ¹³CO ($\Delta E = 35 \text{ K}$), HCO⁺ + ¹³CO \leftrightarrow H¹³CO⁺ + ¹²CO ($\Delta E = 9 \text{ K}$), HCO⁺ + C¹⁸O \leftrightarrow HC¹⁸O⁺ + ¹²CO ($\Delta E = 14 \text{ K}$) and H¹³CO⁺ + C¹⁸O \leftrightarrow HC¹⁸O⁺ + ¹³CO ($\Delta E = 5 \text{ K}$). These reactions, slightly exothermic in the forward direction, were introduced by Langer et al. (1984) because of their capability to cause isotopic fractionation; we used the temperature-dependent reaction rate constants adopted by these authors (Table 3 of their paper).

The library of chemical reactions includes 2142 reactions among 111 species. The set of reactions and species is available on request to the authors.

Finally, as said above, each rotational level of CO (and its isotopes) is considered as a separate chemical species. The rate constants of the destruction reactions, which are involved in Eq. (1), have been assumed identical for all levels, while reactions leading to CO have been assumed to form it in all rotational levels, with an equal probability to form each of them, i.e. p_j^{rs} in Eq. (1) is the same for all j . We used here the simplest conservative hypothesis, although a probability to form each rotational level proportionally to its statistical weight $g_j = 2j + 1$ is also a reasonable assumption.

2.5. Thermal equilibrium

In some of the model calculations presented hereafter, the temperature distribution of the gas throughout the cloud was obtained, in a self consistent way, together with the chemical composition, by solving a thermal balance equation simultaneously with the chemical balance equations.

Under the assumption of steady state equilibrium, the gas temperature is obtained by equating the heating and cooling rates which both depend on position within the cloud. The external heat sources are the galactic cosmic rays and the interstellar UV photons incident on the clouds. Part of their energy is converted into thermal kinetic energy of the gas, either directly through thermalization of electrons ejected after ionization or indirectly through exothermic chemical reactions between atoms, ions and molecules. The gas cools through collisional excitation of the fine structure levels of atoms and ions and of rotational levels of molecules. All the heating and cooling

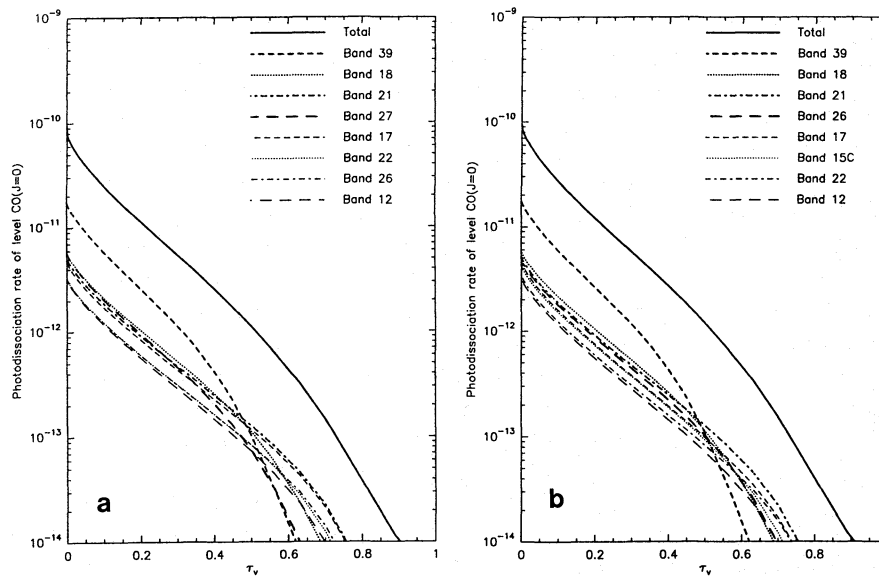


Fig. 1a and b. Photodissociation rate of the CO($J = 0$) level in a translucent cloud model. Contribution of the different bands. Model parameters: $\tau_0 = 2$, $n = 10^3 \text{ cm}^{-3}$ and $T = 25 \text{ K}$. Spectroscopic data **a** from Table 1 and **b** from van Dishoeck & Black (1988)

processes included in our model have been extensively studied in the literature and are presented in Appendix B.

3. Variation of photodissociation rates with depth: contributions of the bands, self-shielding and mutual shielding

In this section we want to discuss how the new spectroscopic data affect the photodissociation rate of CO and its variation with depth and compare with the previous model calculations of VDB. For that purpose, the photodissociation rate of the first rotational level of CO, computed from Eq. (13), is plotted in Fig. 1 versus the optical depth τ_v within a cloud of uniform density ($n = 10^3 \text{ cm}^{-3}$) and temperature ($T = 25 \text{ K}$) which is exposed to the external UV radiation field of Mathis et al. (1983). The cloud has plane parallel geometry of finite thickness; the optical depth from the surface to the mid plane of the cloud, $\tau_v = 2$, corresponds to that of a typical translucent interstellar cloud. The photodissociation rates of individual rotational lines starting from level $J = 0$ are also plotted, at least those that give the main contribution. Our results, using the spectroscopic data listed in Table 1, are plotted in Fig. 1a while Fig. 1b displays the results obtained from our model but with the spectroscopic data adopted by VDB (their Table 1) and also listed in Table 1. The photodissociation rates of the rotational level are very similar in both models, only some line photodissociation rates (e.g. those belonging to the bands 15C, 22, 26 and 27) differ between the two model calculations due to differences in oscillator strengths and, chiefly, in lifetime estimations.

Fig. 1 illustrates an important result already pointed out in our preliminary work (VLER): at low optical depth, photodissociation comes from absorption of photons in the core of the lines so that lines belonging to the bands with the largest oscillator strengths (i.e. bands n° 39, 18, 21, 27 and 17) give the largest contributions to the photodissociation rate; as self-shielding increases with depth within the cloud, beyond $\tau_v \approx 0.5$ for the cloud parameters adopted here, the core of the line becomes

opaque, photodissociation occurs in the line wings so that the lines belonging to the bands with the lowest radiative lifetimes (i.e. bands n° 21, 17, 26 and 12) give the largest contributions to the photodissociation rate.

Furthermore, only the CO lines whose wavelengths lie far enough from H₂ (or H) lines participate to the dissociation. Indeed, at the depth where CO becomes abundant, the column densities of H₂ and H are so large (much larger than those of CO) that shielding by their lines becomes very strong. The lines are heavily saturated, they extend over a few Å apart from the central wavelength, leading to a complete extinction of photons in this wavelength range. This is illustrated in Fig. 2 where we have plotted, in the wavelength range 912–937 Å, the absorbed intensities for CO, ¹³CO, C¹⁸O, H and H₂, computed at $\tau_v = 2$, in the centre of the cloud model defined above. The absorbed intensity is defined as (see Eq. 16):

$$k_x(\lambda, \tau_v) = \exp(-\sum_j N_j^X(\tau_v) \sum_i \sigma_{ji}(\lambda)) \quad (17)$$

where $N_j^X(\tau_v)$ is the column density of level J of species X from the cloud surface to the current point of depth τ_v and the second summation of absorption cross-sections is over all lines starting from level J . A glance at Fig. 2 shows immediately that the lines belonging to the bands 7D, 9A, 13, 14, 15A, 15B will not contribute to the CO photodissociation since they are completely shielded by H₂ lines. This is also the case for bands 19, 24, 31, 33 and 38 lying at wavelengths not represented on the figure.

If shielding of CO lines by H and H₂ lines is very efficient, shielding of lines of the rarer isotopomers ¹³CO and C¹⁸O by CO lines is not efficient. This is clearly demonstrated on Fig. 3 where we have plotted the photodissociation rate of the first rotational level of CO, ¹³CO and C¹⁸O versus the optical depth within the translucent cloud defined above. The decrease of the photodissociation rate of CO, as depth within the cloud increases, is much more rapid than that of ¹³CO, itself slightly

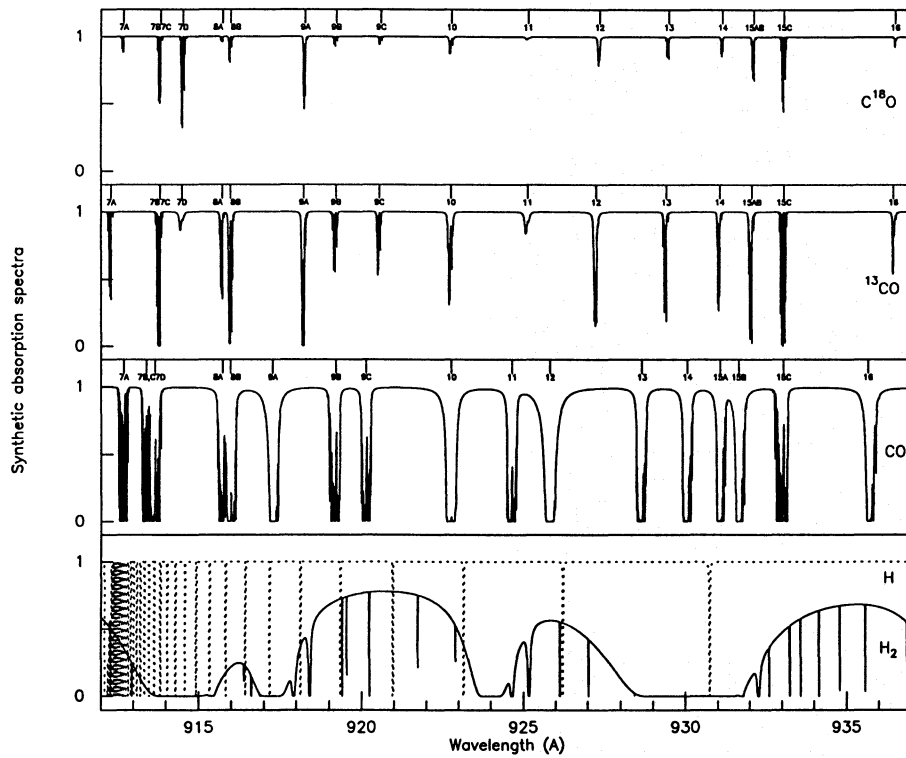


Fig. 2. Absorbed intensity spectra of C^{18}O , ^{13}CO , CO and H_2 in the center ($\tau_v = 2$) of the translucent cloud model defined in Fig. 1. Labels of CO bands correspond to those listed in Table 1

steeper than that of C^{18}O . At $\tau_v = 1$, the photodissociation rates of ^{13}CO and C^{18}O remain an order of magnitude larger than that of CO, whereas similar values would have been obtained if mutual shielding had been efficient. The main reason for this low efficiency can be found in Table 1 where it can be seen that, for most of the bands, the band-head frequencies ν_0 of ^{13}CO and C^{18}O are noticeably shifted with respect to those of CO. The corresponding wavelength shifts of rotational lines is so large that the lines do not overlap and hence do not shield each other. It is however worth noting that shielding of ^{13}CO and C^{18}O by CO becomes efficient when the lines lie close each other, as it is the case for lines belonging to the bands 8A, 8B, 10, 22, 27, 32 and 39 (Table 1). Among these bands, only two of them, bands 27 and 39, contribute efficiently to photodissociation; this is too few for mutual shielding to be efficient. More specifically, transitions with $v' = 0$ tend to have efficient mutual shielding while those with $v' > 0$ do not.

4. Model calculations for diffuse, translucent and dark interstellar clouds

In the model calculations presented hereafter, we have considered the first ten rotational levels of H_2 and of the three isotopomers $^{12}\text{C}^{16}\text{O}$, $^{13}\text{C}^{16}\text{O}$ and $^{12}\text{C}^{18}\text{O}$. The set of the generalized statistical equilibrium equations for all these levels, together with the fine structure levels of C, C^+ and O, have been solved simultaneously with the chemical balance equations and a transfer equation for the penetrating UV radiation, as described in the previous section. As already said, the model only applies to quiescent clouds submitted to moderate UV radiation fields, at most 1000 times more intense than the “standard” field of Mathis et

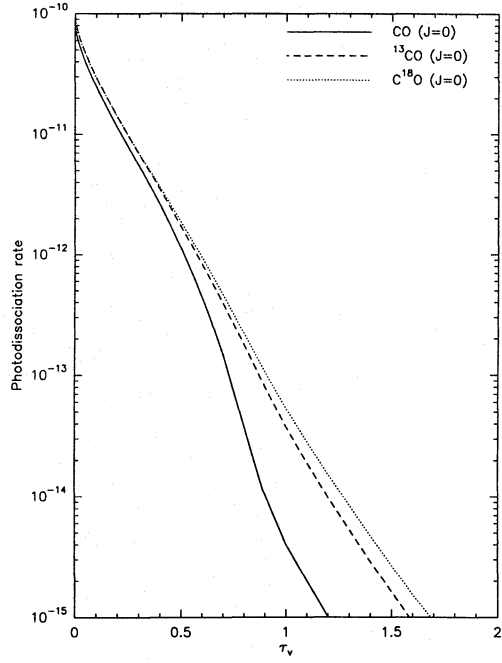


Fig. 3. Photodissociation rates of level of the ($J = 0$) of CO, ^{13}CO and C^{18}O in the translucent cloud model defined in Fig. 1

al. (1983) adopted in all our model calculations. The main reason for this restriction comes from the fact that, in treating the rotational excitation of H_2 (from Viala et al. 1988b), we assumed that the population of the excited vibrational levels ($v'' > 0$) of the ground electronic state is entirely controlled by radiative

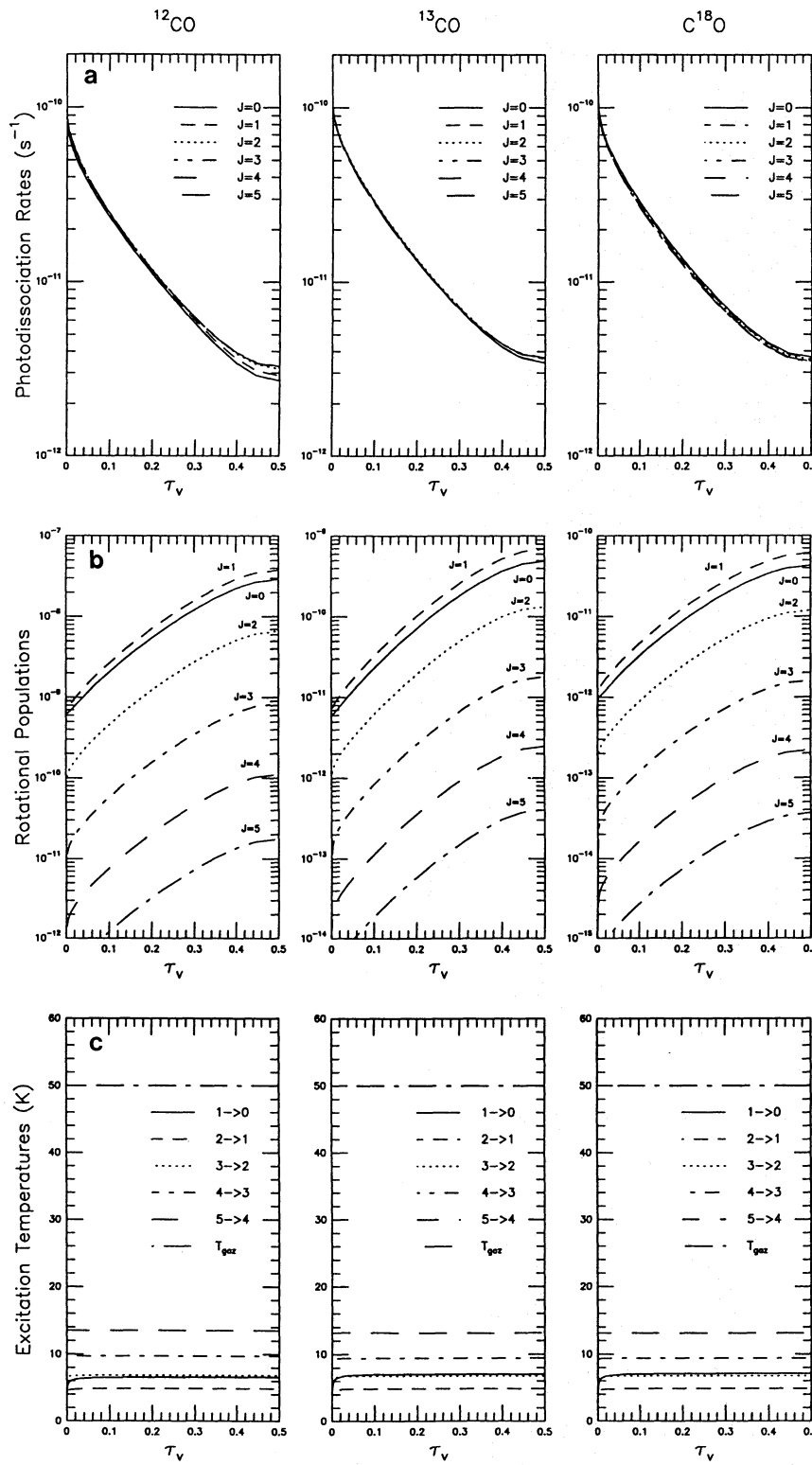


Fig. 4a–c. “Standard” diffuse cloud model: $A_v = 1.1$ magn., $N_H = 2 \times 10^{21} \text{ cm}^{-2}$, $n_H = 500 \text{ cm}^{-3}$, $T = 50 \text{ K}$. Results of model calculations for the three isotopes CO, ¹³CO and C¹⁸O. **a** (top): Photodissociation rates of rotational levels. **b** (middle): Rotational populations $n(J)/n(\text{mol})$. **c** (bottom): Excitation temperatures of the rotational transitions $J \rightarrow J - 1$

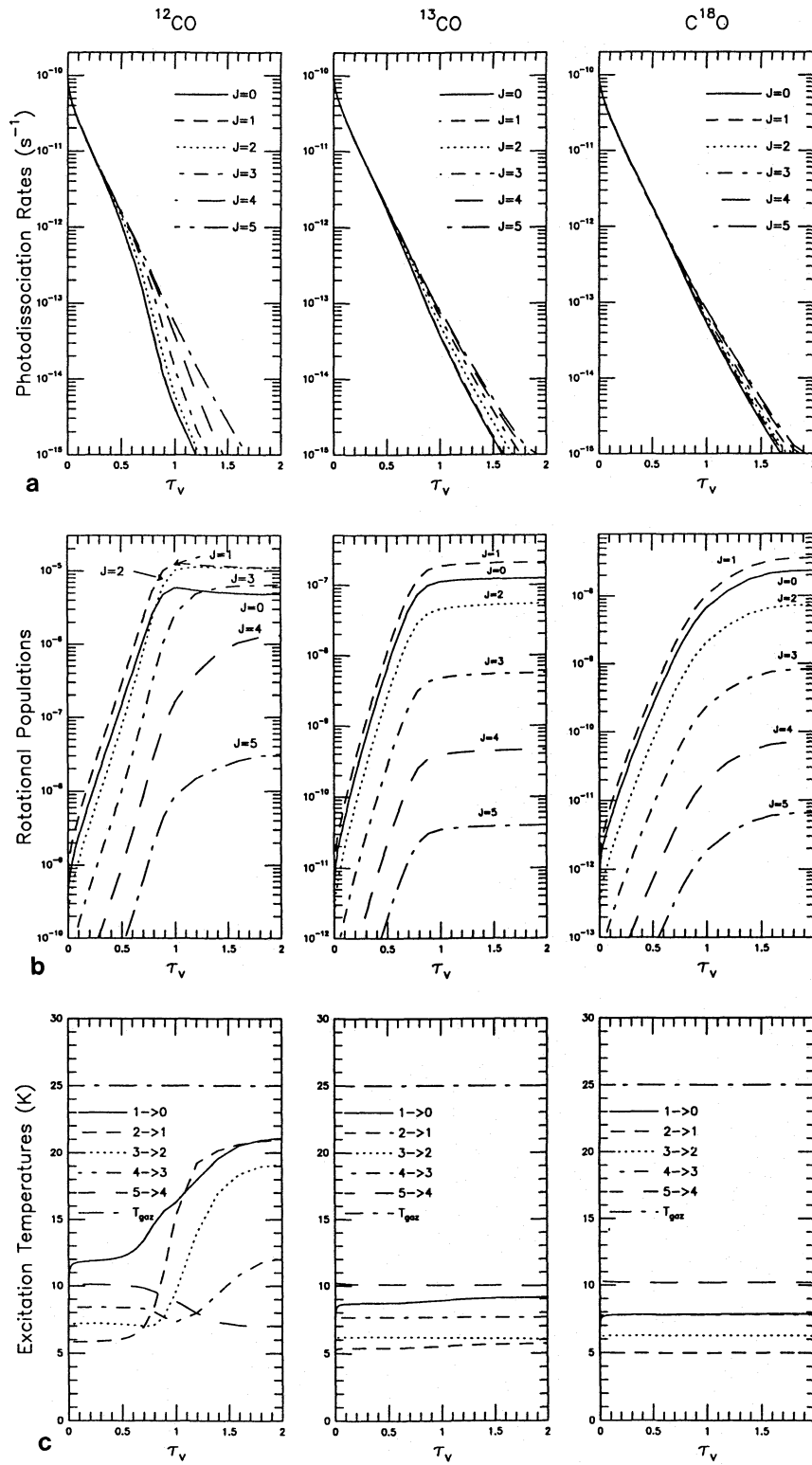


Fig. 5a-c. Same as Fig. 4 for the “standard” translucent cloud model: $A_v = 4.4 \text{ magn.}$, $N_H = 8 \times 10^{21} \text{ cm}^{-2}$, $n_H = 1000 \text{ cm}^{-3}$, $T = 25 \text{ K}$

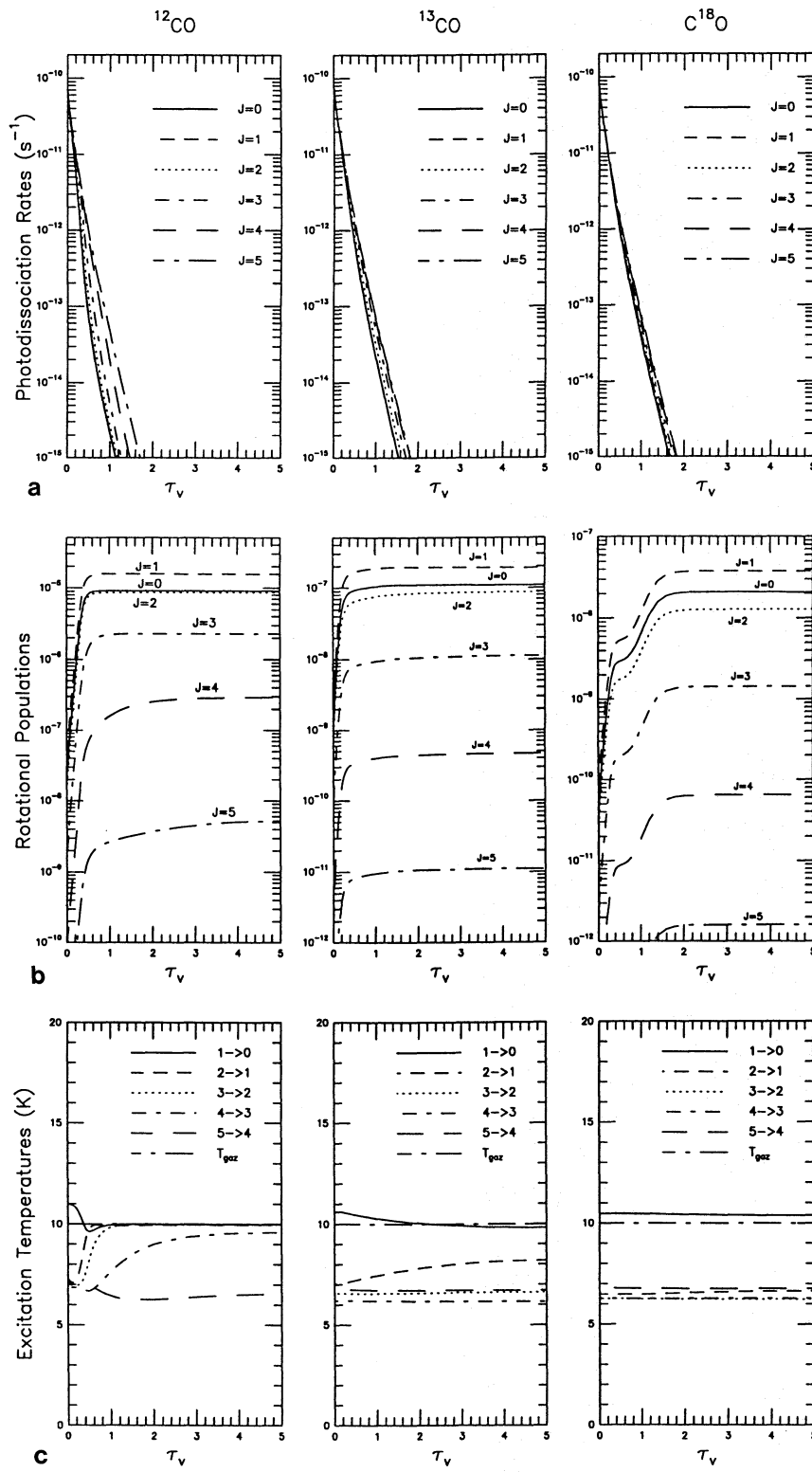


Fig. 6a–c. Same as Fig. 4 for the “standard” dense dark cloud model: $A_v = 10.8$ mag., $N_H = 2 \times 10^{22} \text{ cm}^{-2}$, $n_H = 10^4 \text{ cm}^{-3}$, $T = 10 \text{ K}$

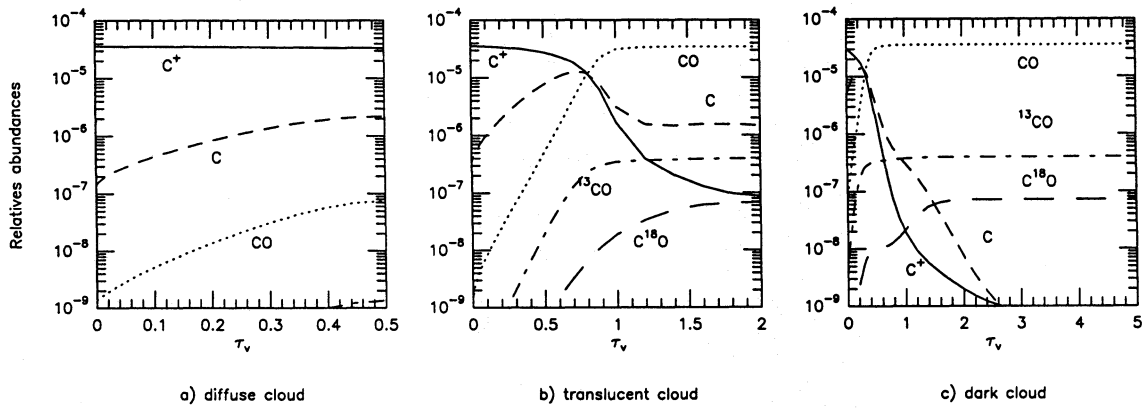


Fig. 7a–c. Fractional abundances $x(s) = n(s)/n_H$ of C, C⁺ and CO in the three isothermal “standard” cloud models

of cloud, as can be deduced or guessed from observations. The standard models have uniform density and temperature. For the elemental abundances, we adopted the solar values from the compilation by Anders & Grevesse (1989), i. e. H:He:C:O:S:Mg:Si:Fe = 1:9.8(-2):3.6(-4):8.5(-4):1.6(-05):3.8(-5):3.5(-5):4.7(-5), with the same depletion factor of 10 for C and O for the three clouds, but an increasing depletion factor for the sulfur and the metals of 10, 100 and 10^4 for the diffuse, translucent and dark cloud, respectively. The adopted isotopic abundances are $^{12}\text{C}/^{13}\text{C} = 90$ and $^{16}\text{O}/^{18}\text{O} = 500$. We also ran three standard models in which the temperature distribution is obtained by solving the thermal balance equation, all other parameters being unchanged. Table 2 gives, for the six standard models, the column densities (relative to the total hydrogen column density) and the rotational or fine structure population (in terms of the ratio of the column density of a particular level to the overall column density of the species under consideration) of H₂, the three CO isotopes and the atomic cooling agents C, C⁺ and O.

Figs. 4, 5 and 6 present, for the standard isothermal diffuse, translucent and dark cloud, respectively, the variations as a function of depth of the photo-dissociation rates (Figs. labeled a) and of the fractional abundances (Figs. b), defined as $x(s) = n(s)/n_H$, for the first rotational levels of CO and its isotopes; the corresponding excitation temperatures of the rotational transitions are plotted in Figs. labeled c. The transition C⁺ → C → CO in the three cloud models is illustrated in Fig. 7.

4.1. Selective rotational photodissociation rates: self-shielding and mutual shielding

The way the self-shielding controls the variations of the photodissociation rates of individual rotational levels with depth is illustrated in Figs. 4a, 5a and 6a.

Firstly, for each isotope, the photodissociation rate $\zeta_J(0)$ of a particular level J at the cloud surface has a value which is nearly independent of the rotational quantum number J . Indeed, from Eq. (13), (14) and (15), and if, to a first approximation, photons

coming from the opposite side of the cloud can be neglected, the rate $\zeta_J(0)$ can be written

$$\zeta_J(0) = \frac{\pi e^2}{m_e c} \sum_{\text{bands } v} \frac{f_{vv'} p_{v'}}{\nu_0(vv')} \times \sum_{JJ' \text{ lines of band } v} \frac{S_J}{2J+1} \nu_{JJ'} (4\pi J(0, \nu_{JJ'})) \quad (18)$$

since the line profile is normalized to unity and since also, to a very good approximation, the external radiation field has a constant value $J(0, \nu_{JJ'})$ over the line and can be removed from the integral of Eq. (13). The first summation is over all vibrational bands leading to excited electronic states (listed in Table 1). For a given isotope, it is the same for all rotational levels that belong to the same vibrational level (in our model calculations all lines start from the ground vibrational level $v = 0$). The second summation is over all lines JJ' within the same band (2 or 3 according to whether it is a $\Sigma \rightarrow \Sigma$ or a $\Sigma \rightarrow \Pi$ transition); the frequencies $\nu_{JJ'}$ (listed in the UV atlas) of lines belonging to the same vibrational band vv' do not greatly differ with the rotational quantum number J , and hence it is also the case for the radiation field $J(0, \nu_{JJ'})$; to a very good approximation the two terms $\nu_{JJ'}$ and $J(0, \nu_{JJ'})$ can be replaced by $\nu_0(vv')$ and $J(0, \nu_0(vv'))$, where $\nu_0(vv')$ is the band head frequency; these two terms can be extracted from the last summation which reduces to the sum within the band of $(S_J/(2J+1))$ which, by definition, is equal to unity. Finally, the rotational photodissociation rate at the cloud surface reduces to

$$\zeta_J(0) = \frac{\pi e^2}{m_e c} \sum_{v'} \frac{f_{vv'} p_{v'} \nu_0(vv')}{\nu_0(vv')} (4\pi J(0, \nu_{vv'})) \quad (19)$$

and is independent of J . Furthermore, as can be seen from Table 1, the band parameters do not greatly differ for the three isotopes, which have a nearly identical unshielded rotational photodissociation rate of 10^{-10} s^{-1} in the UV radiation field of Mathis et al. (1983). This corresponds to an increase by a factor of about 20 and is due to the use of the new spectroscopic data, confirming so the previous results of VLER and VDB.

As the depth within the cloud increases, the radiation field within each rotational line will vary from line to line under the combined influence of self shielding, shielding by neighbouring H and H₂ lines or lines starting from another rotational level and shielding by dust grains. Therefore, the photodissociation rate of each rotational level ζ_J will decrease with depth, in principle in a different way from one level to the other.

In diffuse clouds however, carbon is mainly in the form of C⁺ (Fig. 7a) and CO is only a trace compound with a fractional abundance in the range $1 - 5 \times 10^{-8}$. This is too low for self shielding to be very efficient: the radiation field is attenuated through dust and H and H₂ line absorption so that its variation with depth within the cloud is roughly the same for all CO lines (including isotopes). The rotational photodissociation rate shows essentially the same variation with depth for all rotational levels of the three isotopes.

In the denser and more opaque translucent cloud the CO abundance increases so as to take most of the gas phase carbon in the half inner part of the cloud (Fig. 7b). Self-shielding becomes important, at least for the first four rotational levels $J = 0$ to 3 (Fig. 5b). The main consequence is that the photodissociation becomes selective, i.e. the rotational photodissociation rate and its variation with depth depend on the rotational quantum number J : the more populated the level, the more important the self-shielding and the more rapid is the decrease of the rotational photodissociation rate with depth. This is clearly shown in Fig. 5a for the main isotope. As also shown on the figure, for the rarer isotopes ¹³CO and C¹⁸O, less abundant and hence less efficiently self-shielded, the variations of photodissociation rates with depth are less rapid than for the main isotope, nevertheless, the photodissociation still remains rotationally dependent.

The dark cloud model shows behaviors of photodissociation rates qualitatively and quantitatively similar to those observed in the translucent model (compare Fig. 5a and 6a), i.e. a selective photodissociation with a self-shielding that becomes efficient for nearly all rotational levels of the main isotope. The variation of rotational photodissociation rates with depth is only slightly more rapid than the one observed in the translucent cloud. The decrease is fairly rapid: five order of magnitudes from the surface to $\tau_v = 1$ to 2. This variation with depth is much more rapid than the one which would have been obtained in the case of continuum dissociation (as discussed by VLER) and is due to a higher absorption cross-section in the Doppler core of each rotational line and a correspondingly higher efficiency of self-shielding.

4.2. Selective rotational photodissociation rates: the influence of UV photons on the rotational population of CO

Photodissociation is the main destruction process of CO in regions of the interstellar medium where UV photons are present: this is not surprising apart from the fact that the new spectroscopic data cause a decrease of the overall abundance of CO in diffuse clouds (e.g. the ζ Oph cloud) well below the one observed. This has been already pointed out in the previous models of VLER and VDB. These last authors even showed that, the chemistry

of CO appearing well established, the simplest way to reconcile its computed and observed abundance in diffuse clouds is to assume a reduced value of the interstellar UV radiation field at wavelengths below 980 Å, an hypothesis that cannot be excluded since the interstellar UV field is practically unknown below 1200 Å. The calculations presented here, with a ratio $N(\text{CO})/N_{\text{H}_2} \simeq 5 \times 10^{-8}$ (see Table 2) confirm the difficulty with CO in diffuse clouds. This difficulty disappears in denser and more opaque clouds, where the fairly rapid decrease of the CO photodissociation rate with optical depth leads to column density ratios CO/H₂ (Table 2) of a few 10^{-5} , roughly compatible with observations.

The fact that the photodissociation of CO depends on the rotational level (Sect. 4.1) implies a strong influence of UV photons on its rotational population: this is another important new result of our model calculations, not mentioned in the previous work of VDB. At this point of the discussion, it is worth emphasizing an important difference between the two models. In the VDB's model, the rotational photodissociation rates are computed by assuming that the rotational population of CO is characterized by a single excitation temperature; in other words, the rotational population is not affected by photodissociation. In our calculations this approximation is relaxed: the rotational population is computed by including explicitly, for each level, a destruction term due to photodissociation (see Eq. (1)). Furthermore, if the cloud opacity is large enough, the photodissociation rate of each rotational level varies with depth within the cloud differently from level to level. According to the discussion of Sect. 4.1, this selective rotational photodissociation is a direct consequence of self shielding and implies that, in turn, the photodissociation rates depend on the rotational population. This strong coupling between photodissociation and rotational population is fully accounted for by our model.

Of course, our calculations as well as those performed by VDB, lead to the same overall photodissociation rate of CO, defined as

$$\zeta_{\text{co}}(r) = \sum_J \eta_J(r) \zeta_J(r) \quad (20)$$

where $\eta_J(r) = n_J(r)/n_{\text{co}}(r)$, the population of level J , is assumed by VDB while it is computed by us. Apart from molecular spectroscopic data, the global rate depends only on the UV field and cloud parameters such as the gas and grain density, and not on the way the rotational levels of the molecule are distributed.

The distribution of the rotational population of the three CO isotopomers is plotted in Figs. 4b, 5b and 6b for the three standard isothermal models; the corresponding excitation temperatures of the rotational transitions $J \rightarrow J - 1$ are plotted in Fig. 4c to 6c. As can be seen on these last figures, the assumption of a common constant excitation temperature for all rotational levels is far from reality: $T_{\text{ex}}(J \rightarrow J - 1)$ varies from level to level; for the main isotope, it also varies with position within the cloud, especially in the translucent model. Finally, the excitation temperatures of nearly all transitions of the three isotopes are below the kinetic temperature; only the first transition $J = 1 \rightarrow 0$ of the three isotopes, and the transitions $J = 2 \rightarrow 1$

and $3 \rightarrow 2$ of the main isotope are thermalized in the inner parts of the dark cloud model (Fig. 6c).

Apart from these exceptions, the rotational population of CO and its isotopes is sub-thermally excited under the combined influence of UV photodissociation which destroys the levels and inefficiency of collisions to populate the levels up to thermalization. The separate contribution of both effects is not easy to establish.

In the diffuse cloud model, the rotational photodissociation rates remain large throughout the cloud but nearly independent of J (see Fig. 4a) and the low density does not allow collisions to populate excited levels; both effects add so that the excitation temperatures of the transitions of the three CO isotopes are decreased by factors between 5 and 10 with respect to the true kinetic temperature (see Fig. 4c). The departure from LTE is illustrated in Fig. 8a where we have plotted the population of the first four rotational levels of ^{12}CO throughout the cloud in the exact calculation and by assuming LTE, the overall fractional abundance of CO being the same in both cases. Taking into account self-shielding and rotational selective photodissociation causes drastic changes in the rotational population; as can be seen in Fig. 8a, the net effect is to overpopulate low-lying levels and to underpopulate excited levels with respect to an LTE calculation; indeed, the fractional abundance of level $J = 0$ and 1 is larger in the exact calculation than at LTE, while it is the reverse for levels $J = 2$ and 3. The consequence for the Rayleigh-Jeans brightness temperature of the first three rotational transitions $J = 1 \rightarrow 0, 2 \rightarrow 1$ and $3 \rightarrow 2$ emergent from the cloud surface and obtained from Eq. (8) is illustrated in Fig. 8b; the peak intensities and the line areas integrated over frequency decrease with excitation in the exact calculation while it is the reverse at LTE.

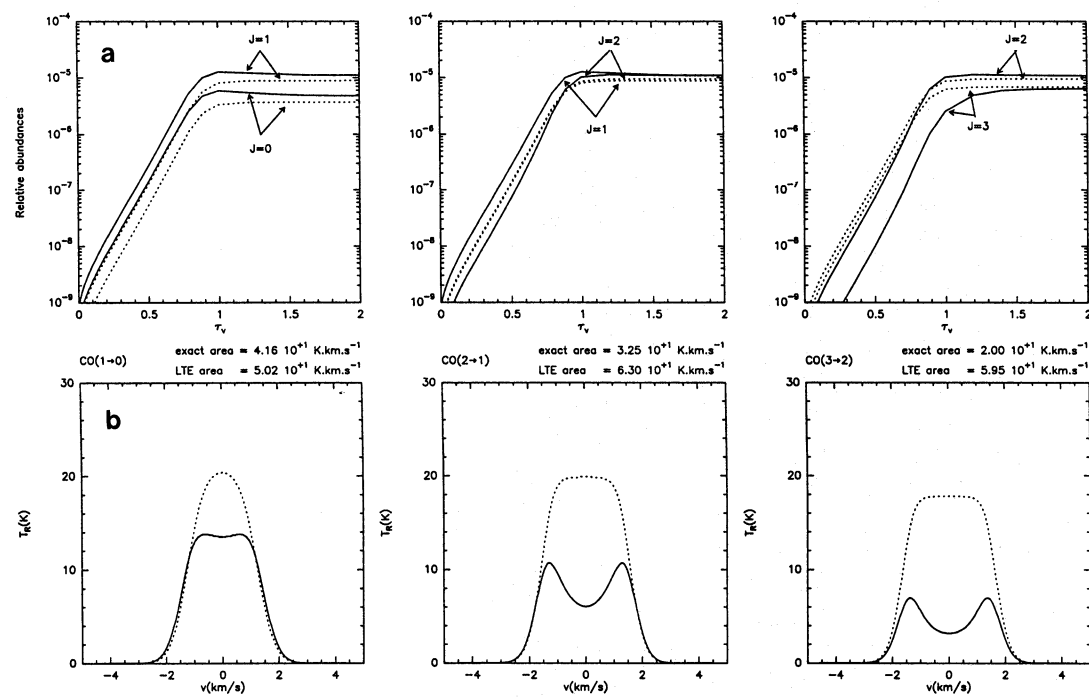
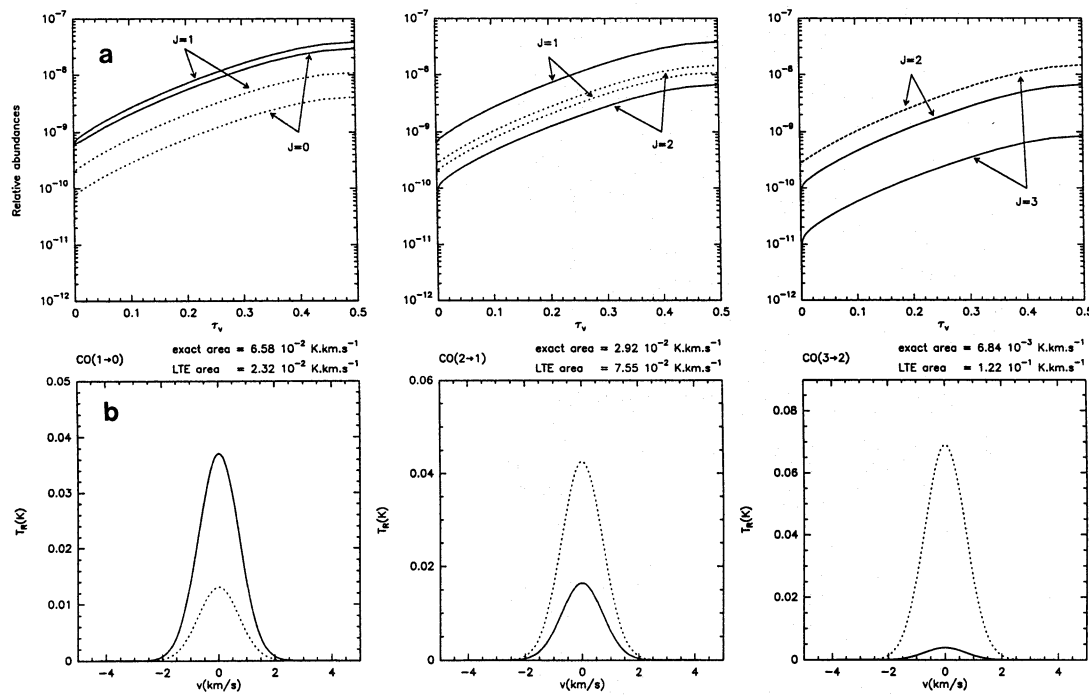
In the translucent cloud model, photo dissociation remains an important destruction process of the isotopes ^{13}CO and C^{18}O , their rotational population of is clearly sub-thermal with T_{ex}/T_{kin} varying in the range 0.2 to 0.4 (see Fig. 5c). Self-shielding becomes efficient for the first four levels of the main isotope, their abundances increase fairly rapidly towards the half inner part of the cloud as do the excitation temperatures of the corresponding transitions (Fig. 5b and 5c). The population of the first four rotational levels in the exact calculation and at LTE and the corresponding Rayleigh-Jeans brightness temperature of the first three rotational transitions of ^{12}CO are plotted in Figs. 9a and 9b, respectively. As a consequence of attenuation of UV photons, departure from LTE decreases from the cloud surface towards the centre where thermalization is nearly achieved (Fig. 5c and 9a). The first three rotational transitions exhibit saturated and self-reversed line profiles (Fig. 9b), as expected from optically thick lines in homogeneous clouds where, as assumed here, the main cause of line broadening is microturbulence (see discussion by Wolfire et al. 1993). Observations of this kind of cloud, e.g. the clouds B157 and L 1075 by Robert & Pagani (1993), show smoother profile, nearly gaussian. This is a general observational feature for interstellar clouds whose opacity becomes significant ($A_v \geq 3 - 4$ mag) and the simplest

way to reproduce these observational data is to assume highly clumpy structure of the cloud.

In the dense dark cloud, thermalization is completely achieved for the first four rotational levels of the main isotope ^{12}CO and $T_{ex} = T_{kin}$ for its first three rotational transitions (Fig. 6c). Thermalization occurs beyond $\tau_v = 1$, in regions where photons participating to the photodissociation of the relevant levels are strongly attenuated and where the adopted density is large enough for collisions to control the excitation. Note however that, for the rare isotopes, only the first rotational transition ($J = 1 \rightarrow 0$) is thermalized, the population of higher levels $J = 2, 3$ remains sub-thermal, with excitation temperatures of excited transitions reduced by nearly a factor 2. It is also worth to emphasize that these lower excitation temperatures $T_{ex}(2 - 1)$ and $T_{ex}(3 - 2)$ for the rare isotopes are only due to an UV photodissociation much more efficient than for ^{12}CO , rates of excitation through collisions being the same for the three isotopes.

Another way to present our model calculations of the rotational population of the three CO isotopes in the three standard isothermal cloud models is illustrated in Fig. 10. For each isotope, we have plotted the quantity $\log(N_J/g_J)$ versus the energy of rotational level J ; N_J is the column density of level J throughout the whole cloud. Three types of calculations have been performed. The first one corresponds to full exact calculation, i.e. resolution of the set of generalized statistical equilibrium equations (1), the resulting column densities N_J are those listed in Table 2. In the second type of calculations, the set of Eqs. (1) have been solved without the photon trapping terms, i.e. by neglecting the absorption and stimulated emission of photons between the levels; this comes back to assume that all lines are optically thin and escape the cloud. The third case assumes an LTE population of the rotational levels, the overall abundance of the three molecules CO, ^{13}CO and C^{18}O are identical to those obtained in the exact calculation (the overall photodissociation rate of CO given by Eq. (20) and all chemical, collisional and radiatives rates are identical in the two cases); the results displayed are the one that would have been obtained by the VDB model.

For high excitation levels the exact calculation leads to column densities N_J systematically lower than the one obtained at LTE. According to the above discussion, this is the result of the combined effect of UV destruction and inefficiency of collisions to thermalize the levels. These two effects act in the same sense; the reduction of N_J with respect to LTE increases with the rotational quantum number: indeed, high excited levels are more difficult to populate through collisions and less shielded from photo-destruction. Whatever the isotope, the departure between the exact calculation and LTE column density values is lower in the dark cloud, where the attenuated UV radiation field and the high density favours excitation so that thermalization is achieved for the first four levels; the adopted density of 10^4 cm^{-3} is however not large enough to thermalize higher levels. Of course, the departure between LTE and the exact calculation increases towards more transparent and diffuse clouds where the excitation conditions becomes less and less favorable. In the translucent



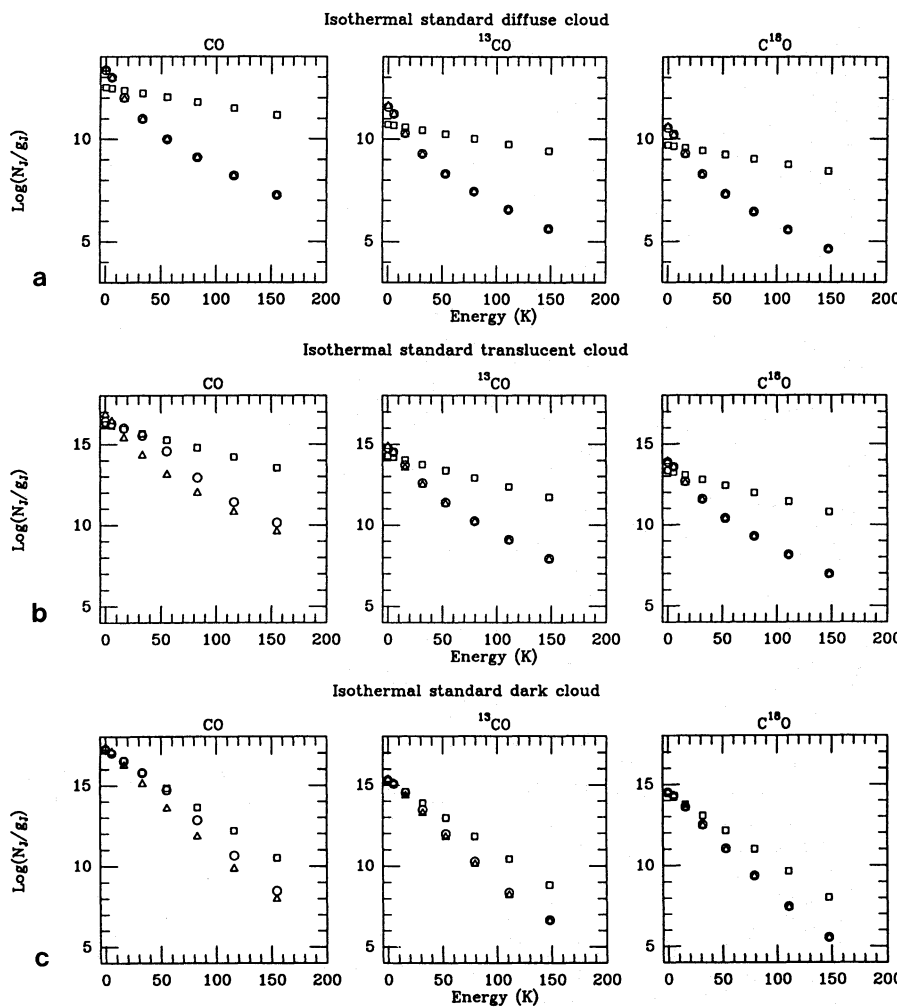


Fig. 10a–c. Column densities, of rotational levels of the three CO isotopes versus their energy in the three isothermal “standard” cloud models. **a** diffuse cloud. **b** translucent cloud. **c** dense dark cloud. Meaning of symbols: \circ : exact calculations. \square : LTE population. \triangle : population obtained by neglecting photon trapping, i.e. absorption and stimulated emission of photons between levels

cloud, thermalization is nearly achieved for the first three levels, even if not completely as discussed above. For higher levels, the reduction of N_J with respect to LTE is much larger than in the dark cloud model. The low density and the presence of UV photons cause an increasing reduction with J of the “exact” column densities with respect to LTE: $N_J(\text{exact})/N_J(\text{LTE}) = 0.2, 1.4 \times 10^{-2}, 1.6 \times 10^{-3}$ and 4.1×10^{-4} for $J = 4, 5, 6$ and 7, respectively. At last, in the diffuse cloud model, the departure between LTE and the exact calculation is the largest, with low lying levels more populated than at LTE and the reverse for excited levels (see above discussion). For ^{12}CO , one gets the following ratio: $N_J(\text{exact})/N_J(\text{LTE}) = 7.2, 3.5, 0.4, 6.0 \times 10^{-2}, 8.5 \times 10^{-3}$ and 2.1×10^{-3} for $J = 0, 1, 2, 3, 4$ and 5.

Another interesting result shown in Fig. 10 concerns the photon trapping: it does not play any role in the rotational excitation of the rarer isotopes ^{13}CO and C^{18}O , and this merely reflects the fact that all lines are optically thin, even in the dark cloud model. The assumption, very often made in analyzing observations, that the lowest excitation lines $J = 1 \rightarrow 0$ and $2 \rightarrow 1$ of ^{13}CO are optically thin appears to be reinforced by our model calculations. For the main isotope however, Fig. 10 clearly indicates that photon trapping play a non negligible role in the rotational excitation of intermediate levels $J = 2$ to 6 in

the translucent and dark clouds: the net effect is an enhancement of the population of these levels, by more than an order of magnitude for levels $J = 3$ to 5.

To conclude this section, we have clearly demonstrated that UV photons, through selective dissociation of rotational levels, can strongly influence the rotational population of CO and its isotopes ^{13}CO and C^{18}O . Hence, in interstellar clouds of moderate opacity or in intense radiation fields, some care must be taken in deriving cloud parameters such as the density and the temperature from analyses of line intensity ratio (e.g. peak or integrated area of the $2 \rightarrow 1/1 \rightarrow 0$ lines), as it is often made. We will return to this point later.

4.3. Thermal equilibrium and temperature distribution

For the three “standard” models whose bulk parameters are given in Table 2 we also performed model calculations in which the thermal balance equation is solved in order to get the gas temperature distribution in a self-consistent way with the chemical composition. The adopted heating and cooling processes are described in Appendix B. The heating rates and the cooling rates throughout the cloud are plotted in Fig. 11a, 11b and 11c for the diffuse, translucent and dark cloud models, respectively. The

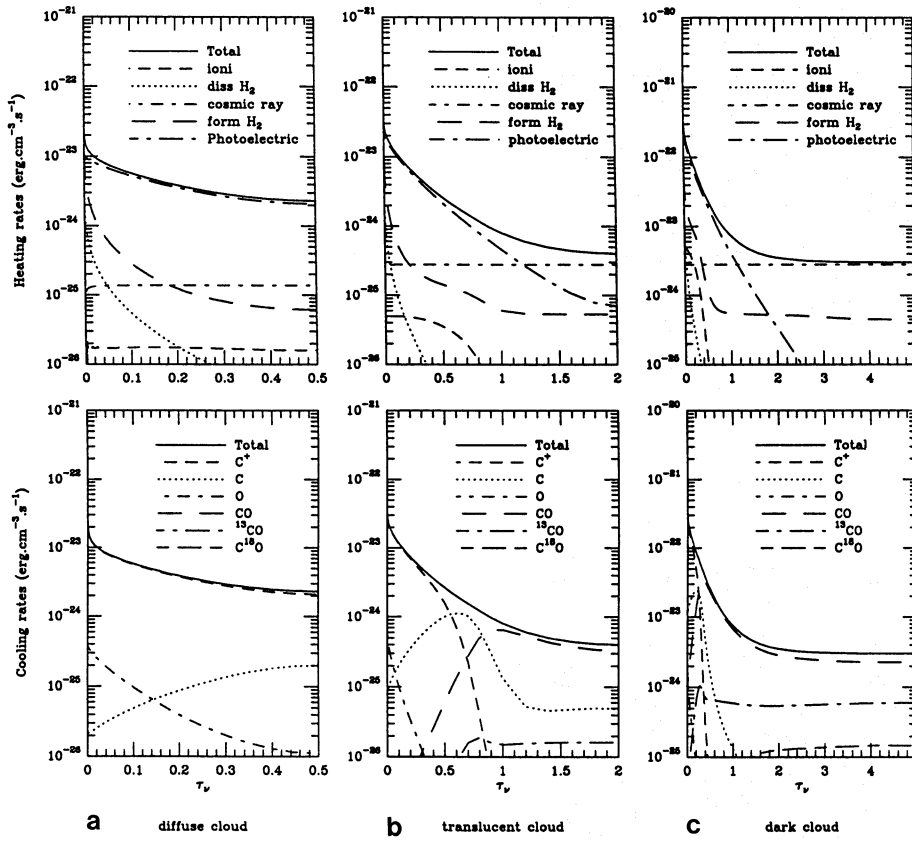


Fig. 11a–c. Cooling and heating rates through out for the three “standard” clouds models: **a** diffuse cloud, **b** translucent cloud, **c** dark cloud

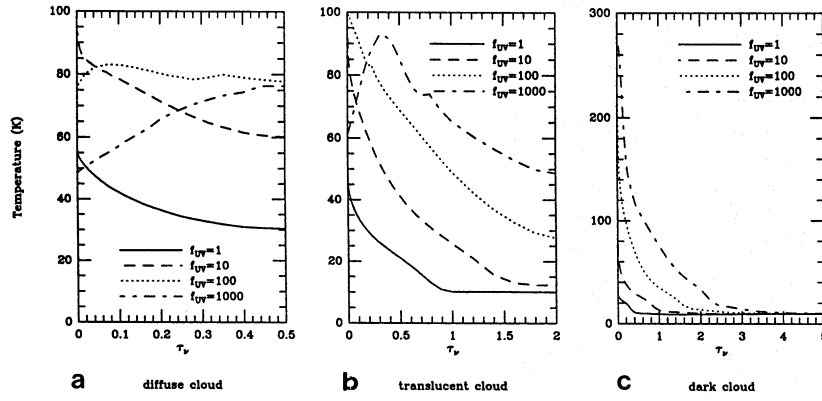


Fig. 12a–c. Gas temperature distribution throughout the three “standard” cloud models with f_{UV} = 1, 10, 100, 1000: **a** diffuse cloud, **b** translucent cloud, **c** dark cloud

corresponding gas temperature distributions are plotted in Fig. 12a to 12c.

Photo-electric emission of electrons from grains is the dominant heating process in regions where UV photons are present, i.e. in diffuse and translucent clouds and in the outer parts of dark clouds. H₂ formation on grains contributes marginally to the heating of the outer parts of diffuse clouds and translucent clouds and of the core of dense dark clouds. In these regions, as well as in the core of translucent clouds, cosmic ray ionization of atomic and molecular hydrogen is the dominant heating process.

The cooling of diffuse clouds is entirely due to the fine structure excitation of ionized carbon. Although more abundant, atomic oxygen gives a much smaller contribution to the cooling because its fine structure levels lies at higher energy than those

of C⁺ and are hence more difficult to excite at the temperature in the range 40–60 K attained in the cloud. In the translucent cloud, the cooling rate is successively due to C⁺, C and ¹²CO excitation, strictly correlated with the abundance distribution of these species shown on Fig. 7b. The gas temperature decreases smoothly from 40 K to 10 K from the surface to τ_v = 1 and then, remains uniform to 10 K in the core of the cloud. This temperature of 10 K, also obtained throughout most parts of the dense dark cloud model (Fig. 12c), fits fairly well what is generally observed in that kind of clouds: according to the model (Fig. 11c), it results from the balance between heating through cosmic ray ionization of H, He and H₂ and cooling due to the rotational excitation of ¹²CO, and, to a lesser extent, of ¹³CO. It is worth noting that the ¹³CO/¹²CO and C¹⁸O/¹²CO cooling rate ratios are ∼0.3 and ∼0.1, respectively, much larger than

the abundance ratios of 0.01 and 2×10^{-3} (see Fig. 7c): this is the effect of photon trapping which causes a drastic reduction of the escape probability, and hence of the cooling efficiency, as the optical depth of the line increases (see Eqs. B10, B6 and B7). The cooling rate by line is much larger for the optically thin lines of C^{18}O than for the optically thick lines of ^{12}CO , cooling rate by this last species however dominates because of its much larger abundance.

Because photo-electric emission from grains is one of the dominant heating process, the gas temperature of interstellar clouds will be very sensitive to the external UV radiation field $J_0(\nu)$. To illustrate this, the temperature distributions computed in the three standard cloud models by multiplying $J_0(\nu)$ by a scaling factor $f_{UV} = 10, 100$ and 1000 , constant with frequency, are also plotted in Fig. 12. As expected, the general trend is an increase of the gas temperature with increasing scaling factor f_{UV} , except for the largest value $f_{UV} = 1000$ in the diffuse and the translucent cloud model, we will return to this later.

At this point of the discussion it is interesting to compare our results with those obtained by LPRF who also performed model calculations including thermal equilibrium. They discussed both constant pressure (isobaric) and constant density (isochoric) models but displayed results for dense clouds alone, so that direct comparison is possible only with their high density isochoric models. The temperature distribution shown in our Fig. 12c and their Fig. 5a displays the same rough qualitative features. The temperature remains more or less uniform, around 10 K , in the half inner part of the cloud for τ_v in the range 2 to 5, and this, whatever the factor f_{UV} . Then, due to UV photo-electric heating, the temperature rises fairly rapidly towards the cloud surface; the larger f_{UV} , the larger and more abrupt is the rise of temperature, which also starts deeper into the cloud. Although qualitatively similar in behaviour, the temperature distributions obtained by LPRF and by us show significant quantitative differences. First, in the outer parts of the cloud, the former are systematically larger than the latter: the surface temperatures in our models are $25, 60, 180$ and 280 K , for $f_{UV} = 1, 10, 100$ and 1000 , respectively, while LPRF obtain $30, 90, 250$ and 900 K . The heating and cooling processes in a dark cloud model with $n = 10^3\text{ cm}^{-3}$ and $f_{UV} = 1000$ are plotted in Fig. 13 and can be directly compared with Fig. 1 of LPRF. The higher temperatures obtained by these authors comes from a larger photo-electric heating rate since they took into account the photo-emission of electrons from PAH, a process not included in our model. Furthermore, the grain photo-electric heating rate computed here is between 2 and 4 times lower than the one computed by LPRF: this is due to differences in grain surface area per unit volume, to a higher intensity of the UV field within the cloud obtained by LPRF who considered only radiation normal to the cloud surface, and, finally, to a different allowance of the saturation of the photo-ejection rate of electrons due to the positive charge taken by the grains. In fact, both models follow the formulation by de Jong (1977, 1980); but, as discussed in appendix B and to allow for variations of the radiation field and grain absorption properties with frequency, we compute explicitly the photo-electric heating rate and the grain

charge by solving simultaneously Eqs. (B1) and (B2), while LPRF adopted the expression of Hollenbach et al. (1991, Eq. B4) obtained with simplifying assumptions on the grain absorption cross-section and the radiation field within the cloud which were assumed independent of frequency. The second difference between LPRF and our model calculations is the small increase of the temperature towards the cloud centre obtained by LPRF while it remains uniform in our models. A glance at the cooling rates (their Fig. 1b and our Fig. 10b) indicates that the small increase of the temperature towards the cloud centre comes from the fact that LPRF neglected cooling by ^{12}CO , which dominates beyond $\tau_v = 4$ and stabilizes the temperature since the abundance of ^{12}CO remains constant, as does the heating rate. LPRF also considered a chemical heating, mainly due to the large exothermicities of the recombination reactions of molecular ions, assuming that the heat of the reaction goes entirely into kinetic energy of the products. This chemical heating is a factor 2 larger than the cosmic-ray heating but remains constant in the core of the cloud. Its introduction in our models, would produce a slightly higher temperature but will not alter its uniformity.

Figs. 12a and 12b show that the temperature distribution throughout the diffuse and the translucent cloud models also begins to increase with the scaling factor f_{UV} , as for the dense dark cloud. This is a direct consequence of the increasing photo-electric heating rate. Nevertheless, the positive charge on grains also increases with the UV radiation field so that, above a critical value of the intensity of this field within the cloud, the ejection rate of photoelectrons saturates and even decreases with increasing UV intensity, because the electrons have more and more difficulty to leave the grain surface. It is this effect, pointed out by de Jong (1977) and discussed in more details by Bel et al. (1989), that finally leads to a decrease of the photo-electric heating rate with increasing UV intensity, above a certain limit, as one approaches the cloud surface. This is well illustrated in Fig. 14 where the photo-electric heating rate throughout the diffuse cloud model is plotted for the four values of the scaling factor f_{UV} . The decrease of the heating rate explains the decrease of the temperature towards the cloud surface, for $\tau_v \leq 0.5$, shown in Fig. 12a and 12b for the diffuse and translucent cloud models submitted to the most intense UV radiation field. Note that the more diffuse the cloud, the more rapidly occurs the saturation of the photo-electric heating: it starts for f_{UV} around a few hundreds for the translucent model and as soon as $f_{UV} = 100$ for the diffuse model, while no saturation occurs for the dense model even with $f_{UV} = 1000$.

While these model calculations were in progress, the problem of the grain photoelectric heating has been re-addressed by Bakes and Tielens (1994) who, among various parameters, considered the influence of the grain size. For very small grains, not considered here, the saturation effect due to grain charge is reduced and the heating efficiency is larger than the one computed here from de Jong's formulation. This could well modify our conclusions about the reduction of the heating efficiency at low optical depth in intense UV fields. New calculations taking

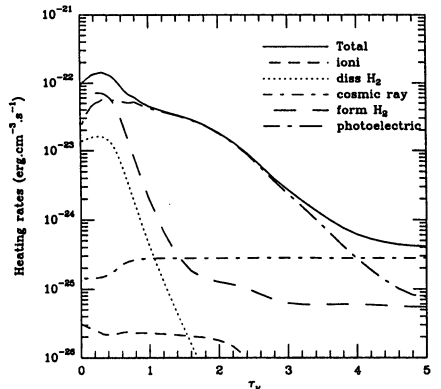


Fig. 13. Heating and cooling rates in a dense dark cloud model with $n = 10^3 \text{ cm}^{-3}$ and $f_{UV} = 1000$

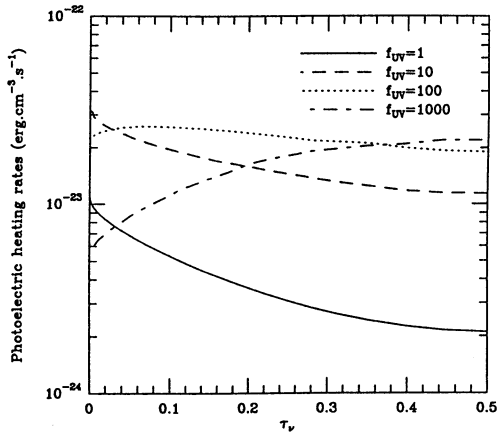


Fig. 14. Effect of the scaling factor of the external radiation field, f_{UV} , on the photo-electric heating rates in the diffuse clouds model

into account the results of Bakes and Tielens (1994) appear to be worthwhile and are planned for the future.

5. Comparison with observations

Rotational lines, mainly the $1 \rightarrow 0$ and $2 \rightarrow 1$ lines, of CO and its isotopes have been observed in a very large variety of clouds in the interstellar medium of our galaxy (and since few years, of external galaxies). Besides observations of individual clouds, systematic surveys of selected areas of the sky have been performed, leading to more or less systematic collection of data such as peak antenna temperatures, line widths and line integrated areas. In some cases, these data are given as function of the visual extinction, which is a measure of the amount of matter along the line of sight and is very useful to check chemical models

5.1. Integrated area of the $1 \rightarrow 0$ line of CO, ^{13}CO and C^{18}O

For that purpose, we have selected three surveys of the $1 \rightarrow 0$ lines of CO, ^{13}CO and C^{18}O in particular molecular clouds. The first one, made by Frerking et al. (1982), concerns the two molecular clouds in Taurus and around ρ Oph with conditions varying from translucent regions ($A_v = 2$ to 4) to fairly dense

and opaque regions ($A_v = 7$ to 20). The second survey by Cericharo and Guélin (1987) concerns less opaque clouds ($A_v = 2$ to 6), again in Taurus. In the third survey of the molecular cloud IC 5146 by Lada et al (1994), a near infrared (JHK bands) photometric survey allowed to sound very opaque regions, up to $A_v = 15$, in which observations of the C^{18}O ($1 \rightarrow 0$) line are available.

We have chosen these three surveys, among many others, because at least two of the three CO isotopes have been observed simultaneously, in a number of points large enough to be statistically significant. Another important reason for this choice comes from the fact that the line integrated area, defined as $I(J \rightarrow J - 1) = \int T_R(J \rightarrow J - 1) dv$ is available. This data, obtained from observations without any assumptions about the physical conditions within the cloud, can be directly compared with our model calculations (Sect. 2.1). It is a better observable than column densities (summed over rotational levels) which are derived quantities often based on assumptions about the population (LTE or LVG).

The line areas $I(1 \rightarrow 0)$ of the three CO isotopes, observed in the three sky areas mentioned above, are plotted versus the visual extinction along the line of sight in Fig. 15a for $0 \leq A_v \leq 5$ and Fig. 15b for $4 \leq A_v \leq 12$. Also plotted in the figures are the line areas obtained in our model calculations. To do this we have run models with various visual extinction, from very diffuse ($A_v = 0.5$) to very opaque ($A_v = 20$) clouds. We have run for series of model with uniform density $n = 10^2, 10^3, 10^4$ and 10^5 cm^{-3} ; for each model, the temperature distribution was computed by solving the thermal balance equation. All computations were made with the element abundances adopted for the standard translucent cloud model, i.e. C and O depleted by a factor of 10, metals and sulfur depleted by a factor of 100 with respect to the solar abundances and isotopic ratios $^{12}\text{C}/^{13}\text{C} = 90$ and $^{16}\text{O}/^{18}\text{O} = 500$. All clouds are exposed to the UV radiation field of Mathis et al. (1983) with no enhancement factor.

A first glance at Figs. 15 shows a fairly large scattering of the observational data among the three surveys. Part of this scattering comes from the uncertainty attached to the determination of visual extinctions, whatever the method used to derive them (star counts or near IR photometry). But the scattering probably also reflects a variety of physical conditions leading to differences in molecular abundances and excitation conditions

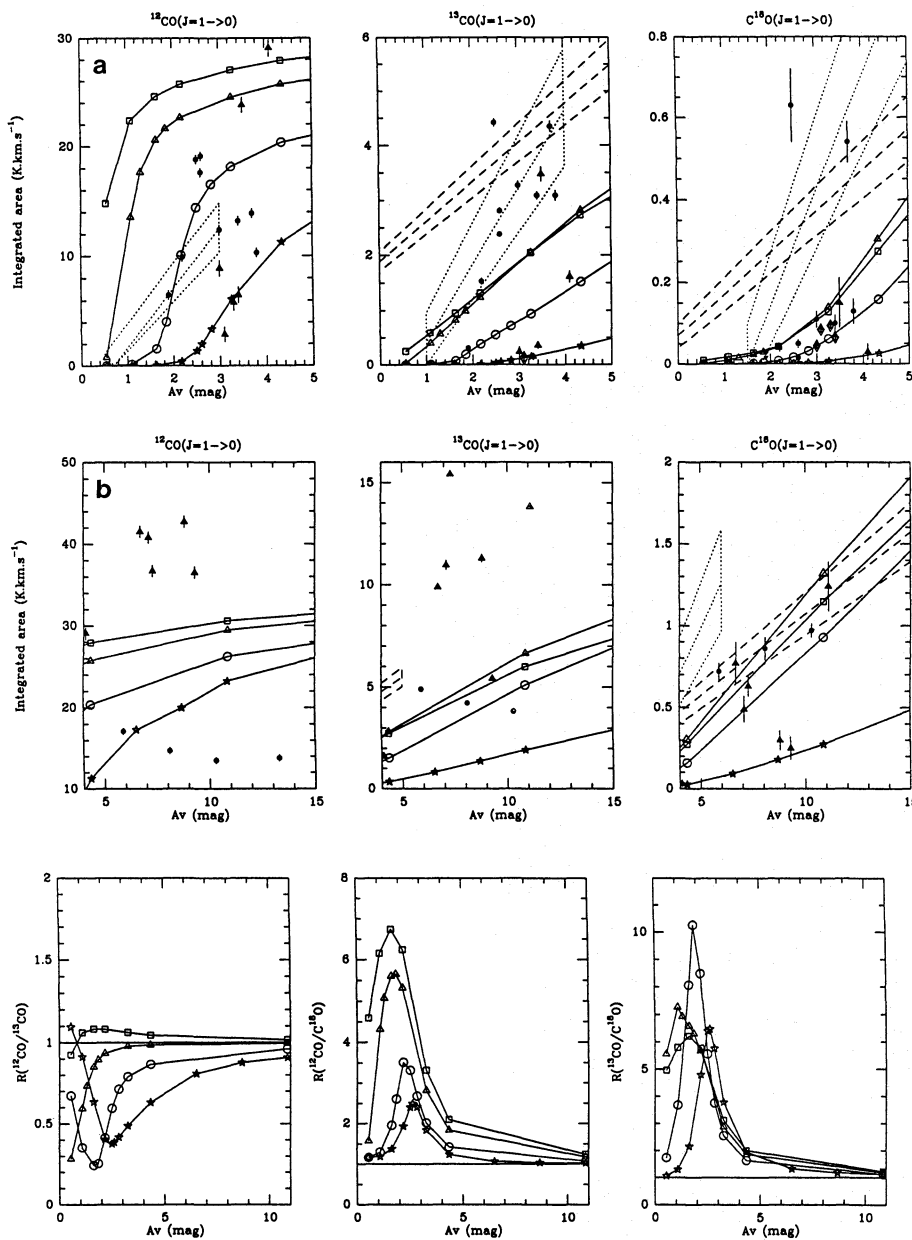


Fig. 15a and b. Integrated areas of the 1-0 lines of CO and its isotopes in interstellar clouds versus the visual extinction A_v in the range $A_v = 0$ to 5 mag and **b** in the range $A_v = 4$ to 12 mag. Full curves correspond to model calculations of uniform clouds with densities $n = 10^2$ (stars), $n = 10^3$ (circle), 10^4 (triangle), 10^5 cm^{-3} (square), in which the temperature distribution is obtained by solving the thermal balance equation. The full symbols represent observations by Frerking et al. (1982) of the Taurus (full circle) and the ρ Oph (full triangle) molecular clouds. Errors bars are also given; arrows represent upper limits. The dotted lines represent observations of the HCL2 molecular cloud by Cernicharo & Guélin (1987). The dashed lines represent observations of the IC5146 molecular cloud by Lada et al. (1994). For both series of observations, the three curves give the linear correlation derived for the sample of observational points together with upper and lower limits

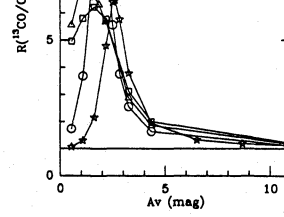


Fig. 16. Computed column density ratios normalized to the isotopic ratios versus the visual extinction. Full curves correspond to model calculations of uniform clouds with densities $n = 10^2$ (stars), 10^3 (circle), 10^4 (triangle), 10^5 cm^{-3} (square) in which the temperature distribution is obtained by solving the thermal balance equation

again towards unity at large A_v where chemical reactions controls the CO abundances. At low A_v and intermediate densities in the range $10^2 - 10^3 \text{ cm}^{-3}$, the larger the density, the lower the cloud temperature; this favours conversion from ^{12}CO to ^{13}CO and explains the more rapid the decrease of $R(^{12}\text{CO}/^{13}\text{CO})$. The maximum enhancement of ^{13}CO with respect to ^{12}CO lies in the range 2-5 and occurs at a visual extinctions that slightly decreases from $A_v = 3$ at $n = 10^2 \text{ cm}^{-3}$ to $A_v = 1.7$ at $n = 10^3 \text{ cm}^{-3}$ and down to $A_v = 0.5$ at $n = 10^4 \text{ cm}^{-3}$. At the highest density of 10^5 cm^{-3} envisaged in our model calculations, the formation of CO molecules is so efficient and occurs so close to the cloud surface that self-shielding and selective photodissociation becomes dominant: as for C^{18}O , but to a lesser extent, the ratio increases with A_v . To summarize, the complex dependence of the ^{13}CO to ^{12}CO abundance ratio on both density, tempera-

ture and cloud opacity, and, of course, element abundance and UV radiation field, the influence of which has not been studied here, shows that all situations from enhancement and depletion of this abundance ratio can be found in the interstellar medium, even for clouds of the same opacity class, especially for diffuse and translucent clouds.

To end with isotopic ratios, let us compare the normalized ratio $R(^{13}\text{CO}/\text{C}^{18}\text{O})$ computed here and plotted in Fig. 16 with the one derived by Lada et al. (1994) in their survey of the IC 5146 molecular cloud and shown in Fig. 19 of their paper. In the range of visual extinctions $A_v \leq 12$ where the comparison is possible, the qualitative agreement between the model and the observations is fairly good: as for the $R(^{12}\text{CO}/^{13}\text{CO})$ ratio, after a rapid rise with increasing A_v , the ratio $R(^{13}\text{CO}/\text{C}^{18}\text{O})$ reaches a maximum and then decreases towards unity. Quantit-

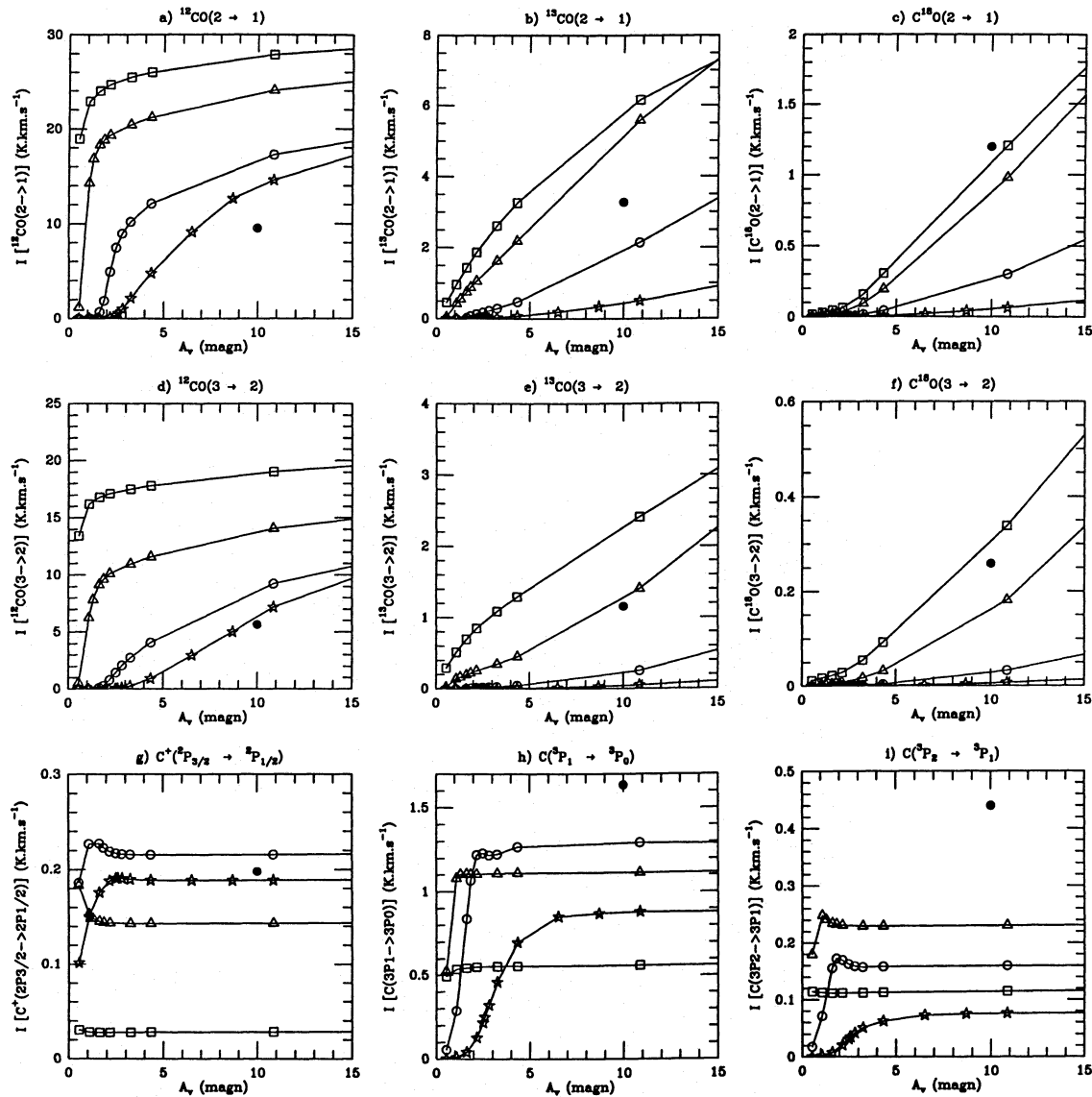


Fig. 17a–i. Predicted line integrated areas (K km s^{-1}) versus the visual extinction. Full curves correspond to model calculations of uniform clouds with densities $n = 10^2$ (stars), 10^3 (circle), 10^4 (triangle), 10^5 cm^{-3} (square) in which the temperature distribution is obtained by solving the thermal balance equation. Full circle represents the prediction of the isochoric model of Le Bourlot et al. (1993) with $n=10^4 \text{ cm}^{-3}$

tatively however there are some differences between theory and observations in the sense that the observed maximum occurs at a larger visual extinctions $A_v = 5$ and is lower, around 3, than the computed one which occurs in the range $A_v = 1-3$ and reaches values between 5 and 10, depending on the density. Furthermore the observed ratio exhibits a second maximum around $A_v = 17$ that does not occur in our model calculations. A higher radiation field than the one used here, leading to a higher temperature and a reduced enhancement of ^{13}CO together with a deeper transition zone for the CO formation would help in reducing the discrepancy.

5.3. Predicted emissivities of CO, C and C^+ lines

To conclude this paper, we want to present our model predictions for the emissivities of the first rotational transitions of the three CO isotopomers and of the fine structure transitions of C and C^+ . The emissivity of the O lines are very low, around $10^{-4} \text{ K km s}^{-1}$ and are not plotted. All these lines, lying in the millimeter and sub-millimeter range, contribute more or less efficiently to the cooling of the gas. Tentative detections of some of them will be undertaken through orbiting experiments (ISO, ODIN...). These predicted emissivities (see Sect. 2.1), that could help to prepare or interpret these observations, or other ones that could also be made on balloon-borne experiments or from the ground, are given in graphical form in Figs. 17a to i. For each line, the emissivity from the whole cloud is plotted ver-

sus its visual extinction. All emissivities are given in K km s^{-1} more commonly used in radioastronomy and be converted in the more conventional unit of $\text{erg cm}^{-2} \text{s}^{-1} \text{sr}^{-1}$ by using the Rayleigh-Jeans relation (9) above. For purpose of comparison, the emissivities computed by LPRF in their standard isochoric model with $n = 10^4 \text{ cm}^{-3}$ are also plotted in the figures. It is beyond the scope of this paper to study individual clouds for which a few observations of some of these lines are available; this is planed for future work.

6. Conclusion

A comprehensive model of the chemistry and rotational excitation of H_2 , CO and its isotopes ^{13}CO and C^{18}O in interstellar clouds has been developed. The model applies to quiescent molecular clouds (diffuse, translucent and dark ones) submitted to a not too intense UV radiation field. The rotational excitation is controlled by chemical processes, including rotational selective photo-dissociation, collisional and radiative processes. For H_2 , UV pumping through excited electronic states is also taken into account. The chemical scheme involves the simplest C and O bearing molecules and their ^{13}C and ^{18}O isotopic substitutions. In some models the gas and grain temperature distributions are obtained by solving the thermal balance equations for each component. Our main conclusions can be summarized as follow:

- Self-shielding controls the variation of photodissociation rates with depth within the cloud. CO lines are strongly shielded by heavily saturated H_2 lines, while, because of fairly large shifts in frequency for most of the bands, shielding of ^{13}CO and C^{18}O lines by CO lines is not efficient.
- The fact that self-shielding is important implies a selective rotational photodissociation. The variation of the photodissociation rates with depth within the cloud strongly depends on the rotational quantum number J : the more populated the level the more efficient is the self-shielding and the more rapid is the decrease of its photodissociation rate. This effect is more pronounced for low-lying levels than for excited one, for the main isotope than for the rarer ones; it is also more important in translucent and dark clouds than in diffuse.
- This strong coupling between photodissociation and rotational excitation has for main consequence to overpopulate low-lying levels and to underpopulate excited levels with respect to an LTE calculation.
- Therefore, the assumption of a common constant excitation temperature for all CO rotational transitions is far from reality. The excitation temperatures of all transitions are lower than the kinetic temperature except for the $J = 1 \rightarrow 0$ of the three isotopes and the $J = 2 \rightarrow 1$ and $J = 3 \rightarrow 2$ transitions of the main isotope in dark cloud models. Furthermore, in the diffuse and translucent cloud models, the peak intensities and the line areas integrated over frequency decrease with line excitation in the exact calculation while it is the reverse at LTE.
- In terms of column densities of rotational levels, the departure between the exact and the LTE rotational population increases with the rotational quantum number J and increases also from dense dark clouds to diffuse clouds. This occurs under the combined influence of rotational selective photodissociation and inefficiency of collisions to populate the level.
- The photon trapping plays no role in the rotational excitation of the rare isotopes ^{13}CO and C^{18}O : this reflect the fact that the lines are optically thin, even in the dark cloud model. This is however no more the case for the lines of the main isotope, in translucent and dark clouds and dark cloud models where the net effect of photon trapping is to increase the population of the $J = 3$ to 5 levels by more than an order of magnitude.
- Photo-electric emission of electrons from grains is the dominant heating process in regions where UV photons are present, i.e. in diffuse and translucent clouds and in the outer parts of dark clouds. It is replaced by cosmic ray ionization of atomic and molecular hydrogen as a dominant heating process in the core of dark clouds. The cooling efficiency is entirely correlated to the cloud composition, with cooling dominated by fine structure excitation of C^+ and rotational excitation of CO in diffuse and dark clouds, respectively; fine structure excitation of C contributes to the cooling of translucent clouds.
- The temperature distribution is strongly dependent on the external UV radiation field: it begins to increase with the UV field, due to enhancement of the photo-electric rate. Above a critical value of the radiation field, the ejection rate of photoelectrons saturates as the positive charge of the grains increases, reducing the efficiency of photo-electric heating so that the gas temperature would decrease again in the absence of another heating process.
- Check of our model calculation have been done through comparison with selected CO surveys of molecular clouds by Frerking et al. (1982), Cernicharo & Guélin (1987) and Lada et al. (1994). The model predicts emissivities of the $1 \rightarrow 0$ line of CO well below the observations with the exception of the $\text{C}^{18}\text{O}(1 \rightarrow 0)$ line in the the molecular clouds surveyed by Frerking et al. (1982) for which agreement between theory and observations is very good. This is the direct consequence of the enhanced photodissociation rates that result from the use of the news spectroscopic data.
- Although the model predicts too low abundances of both ^{13}CO and C^{18}O , the column density ratio $R(^{13}\text{CO}/\text{C}^{18}\text{O})$ normalized to the isotopic ratio that we compute is in fairly good qualitative agreement with the one derived by Lada et al. (1994) in the IC 5146 molecular cloud.

Acknowledgements. All the computations presented in this paper were performed at the “Centre de Calcul Intensif de l’Observatoire de Grenoble”. We thank the computer scientists of the observatory of Grenoble for their maintenance and up-grade of the computers.

- Bally J. and Langer W.D. 1982, ApJ 255, 143
 Bel N., Lafon J.P.J., Viala Y.P., Loireleux E. 1989, A&A 208, 331
 Berrington K.A. 1988, J. Phys. B: Atom. Mol. Phys. 21, 1083
 Cernicharo J. and Guélin M. 1987, A&A 176, 299
 Chu Y.H. and Watson W.D. 1983, ApJ 267, 151
 Clavel J., Viala Y.P., Bel N. 1978, A&A 65, 435
 de Jong T., Chu S.I., Dalgarno A. 1975, ApJ 199, 69
 de Jong T. 1977, A&A 55, 137
 de Jong T. 1980, A&A 91, 68
 Drabbels M., Heinze J., ter-Meulen J.J., Meerts W.L., J. Chem. Phys. 99, 5701
 Draine B.T. 1978, ApJS 36, 595
 Eidelsberg M. and Rostas F. 1990, A&A 235, 472
 Eidelsberg M., Benayoun J.J., Viala Y.P., Rostas F. 1991, A&AS 90, 231
 Eidelsberg M., Benayoun J.J., Viala Y.P., Rostas F., Smith P.L., Yoshino K., Stark G., Shettle C.A. 1992, A&A 265, 839
 Federman S.R., Glassgold A.E., Kwan J. 1979, ApJ 227, 466
 Flower D.R., Launay J.M. 1977, J. Phys. B: Atom. Mol. Phys. 10, 3673
 Flower D.R. and Launay J.M. 1985, MNRAS 214, 271
 Frerking M.A., Langer W.D., Wilson R.W. 1982, ApJ 262, 590
 Glassgold A.E., Huggins P.J., Langer W.D. 1985, ApJ 290, 615
 Glassgold A.E. and Langer W.D. 1973a, ApJ 179, L147
 Glassgold A.E. and Langer W.D. 1973b, ApJ 186, 859
 Glassgold A.E. and Langer W.D. 1974, ApJ 193, 73
 Green S. and Chapman S. 1978, ApJS 37, 169
 Green S., Ramaswamy R., Rabitz H 1978, ApJS 36, 483
 Green S. and Thaddeus P. 1976, ApJ 205, 766
 Green S. and Thrular D.G. 1979, ApJL 231, L101
 Hollenbach D.J., Takahashi T., Tielens A.G.G.M. 1991, ApJ 337, 192
 Jacquet et al. 1992, J. Phys. BA Atom. Mol. Opt. Phys. 25, 285
 Johnson C.T., Burke P.G. et al. 1987, J. Phys. B: Atom. Mol. Phys. 20, 2553
 Lada C.J., Lada E.A., Clemens D.P., Bally J. 1994, ApJ 429, 694
 Langer W.D., Graedel T.E., Frerking M. and Armentrout P.B. 1984, ApJ 277, 581
 Launay J.M. and Roueff E. 1977a, J. Phys. B: Atom. Mol. Phys. 10, 879
 Launay J.M. and Roueff E. 1977b, A&A 56, 289
 Le Bourlot J., Pineau des Forêts G., Roueff E., Flower D.R. 1993, A&A 267, 233
 Letzelter C., Eidelsberg M., Rostas F., Breton J., Thieblemont B. 1987, Chem. Phys. 114, 273
 Levelt P.F., Ubachs W., Hogervorst W. 1992a, J. Phys. II (France) 2, 801
 Levelt P.F., Ubachs W., Hogervorst W. 1992b, J. Chem. Phys. 97, 7160
 Mamon G.A., Glassgold A.E., Huggins P.J. 1988, ApJ 328, 797
 Mathis J.S., Mezger P.G., Panagia N. 1983, A&A 128, 212
 Monteiro and Flower D.R. 1987, MNRAS 228, 101
 Morton D.C. and Noreau L. 1994, ApJS 95, 301
 Nercessian E., Guilloteau S., Omont A., Benayoun J.J. 1989, A&A 210, 225
 Robert C. and Pagani L. 1993, A&A 271, 282
 Roueff, E. 1990, Molecular Astrophysics, Hartquist T.W. eds, p 254
 Roueff E. and Le Bourlot J 1990, A&A 236, 515
 Rybicki G.B. 1984, in Methods in radiative transfer, ed. W Kalkofen, Cambridge, University Press, p. 21
 Schröder et al. 1991, J. Phys. B: Atom. Mol. Phys. 24, 2487
 Spitzer L. Jr 1949, ApJ 109, 337
 Spitzer L. Jr 1968, Diffuse matter in space, Wiley Interscience, New York
 Spitzer L. Jr and Tomasko M. G. 1968, ApJ 152, 971
 Staemmler V. and Flower D.R. 1991, J. Phys. B: Atom. Mol. Opt. Phys. 24, 2343
 Stark G., Yoshino K., Smith P.L., Ito K., Parkinson W.H. 1991, ApJ 369, 574
 Stark G., Smith P.L., Ito K. and Yoshino K. 1992, ApJ 395, 705
 Stark G., Yoshino K., Smith P.L., Esmond J.R., Ito K. and Stevens H.H. 1993, ApJ 410, 837
 van Dishoeck E.F. and Black J.H. 1988, ApJ 334, 802 (VDB)
 Viala Y.P. 1986, A&AS 64, 391
 Viala Y.P., Letzelter C., Eidelsberg M., Rostas F 1988 a, A&A 193, 265 (VLER)
 Viala Y.P., Roueff E., Abgrall H. 1988 b, A&A 190, 215
 Wolfire M.G., Hollenbach D., Tielens A.G.G.M. 1993, ApJ 402 195
 Yoshino K., Stark G., Smith P.L., Parkinson W.H., Ito K. 1988, J. de Phys. Suppl. N° 3, C1-37
 Yoshino K., Stark G., Esmond J.R., Smith P.L., Ito K. and Matsui T. 1995, ApJ 438, 1013

This article was processed by the author using Springer-Verlag \LaTeX
 A&A style file version 3.